Measurement of the anomalous like-sign dimuon charge asymmetry with 9 fb^{-1} of $p\bar{p}$ collisions

V. M. Abazov,[35] B. Abbott,[73] B. S. Acharya,[29] M. Adams,[49] T. Adams,[47] G. D. Alexeev,[35] G. Alkhazov,[39] A. Alton,[61,*] G. Alverson,[60] G. A. Alves,[2] M. Aoki,[48] M. Arov,[58] A. Askew,[47] B. Åsman,[41] O. Atramentov,[65] C. Avila,[8] J. BackusMayes,[80] F. Badaud,[13] L. Bagby,[48] B. Baldin,[48] D. V. Bandurin,[47] S. Banerjee,[29] E. Barberis,[60] P. Baringer,[56] J. Barreto,[3] J. F. Bartlett,[48] U. Bassler,[18] V. Bazterra,[49] S. Beale,[6] A. Bean,[56] M. Begalli,[3] M. Begel,[71] C. Belanger-Champagne,[41] L. Bellantoni,[48] S. B. Beri,[27] G. Bernardi,[17] R. Bernhard,[22] I. Bertram,[42] M. Besançon,[18] R. Beuselinck,[43] V. A. Bezzubov,[38] P. C. Bhat,[48] V. Bhatnagar,[27] G. Blazey,[50] S. Blessing,[47] K. Bloom,[64] A. Boehnlein,[48] D. Boline,[70] E. E. Boos,[37] G. Borissov,[42] T. Bose,[59] A. Brandt,[76] O. Brandt,[23] R. Brock,[62] G. Brooijmans,[68] A. Bross,[48] D. Brown,[17] J. Brown,[17] X. B. Bu,[48] M. Buehler,[79] V. Buescher,[24] V. Bunichev,[37] S. Burdin,[42,†] T. H. Burnett,[80] C. P. Buszello,[41] B. Calpas,[15] E. Camacho-Pérez,[32] M. A. Carrasco-Lizarraga,[56] B. C. K. Casey,[48] H. Castilla-Valdez,[32] S. Chakrabarti,[70] D. Chakraborty,[50] K. M. Chan,[54] A. Chandra,[78] G. Chen,[56] S. Chevalier-Théry,[18] D. K. Cho,[75] S. W. Cho,[31] S. Choi,[31] B. Choudhary,[28] S. Cihangir,[48] D. Claes,[64] J. Clutter,[56] M. Cooke,[48] W. E. Cooper,[48] M. Corcoran,[78] F. Couderc,[18] M.-C. Cousinou,[15] A. Croc,[18] D. Cutts,[75] A. Das,[45] G. Davies,[43] K. De,[76] S. J. de Jong,[34] E. De La Cruz-Burelo,[32] F. Déliot,[18] M. Demarteau,[48] R. Demina,[69] D. Denisov,[48] S. P. Denisov,[38] S. Desai,[48] C. Deterre,[18] K. DeVaughan,[64] H. T. Diehl,[48] M. Diesburg,[48] P. F. Ding,[44] A. Dominguez,[64] T. Dorland,[80] A. Dubey,[28] L. V. Dudko,[37] D. Duggan,[65] A. Duperrin,[15] S. Dutt,[27] A. Dyshkant,[50] M. Eads,[64] D. Edmunds,[62] J. Ellison,[46] V. D. Elvira,[48] Y. Enari,[17] H. Evans,[52] A. Evdokimov,[71] V. N. Evdokimov,[38] G. Facini,[60] T. Ferbel,[69] F. Fiedler,[24] F. Filthaut,[34] W. Fisher,[62] H. E. Fisk,[48] M. Fortner,[50] H. Fox,[42] S. Fuess,[48] A. Garcia-Bellido,[69] V. Gavrilov,[36] P. Gay,[13] W. Geng,[15,62] D. Gerbaudo,[66] C. E. Gerber,[49] Y. Gershtein,[65] G. Ginther,[48,69] G. Golovanov,[35] A. Goussiou,[80] P. D. Grannis,[70] S. Greder,[19] H. Greenlee,[48] Z. D. Greenwood,[58] E. M. Gregores,[4] G. Grenier,[20] Ph. Gris,[13] J.-F. Grivaz,[16] A. Grohsjean,[18] S. Grünendahl,[48] M. W. Grünewald,[30] T. Guillemin,[16] F. Guo,[70] G. Gutierrez,[48] P. Gutierrez,[73] A. Haas,[68,‡] S. Hagopian,[47] J. Haley,[60] L. Han,[7] K. Harder,[44] A. Harel,[69] J. M. Hauptman,[55] J. Hays,[43] T. Head,[44] T. Hebbeker,[21] D. Hedin,[50] H. Hegab,[74] A. P. Heinson,[46] U. Heintz,[75] C. Hensel,[23] I. Heredia-De La Cruz,[32] K. Herner,[61] G. Hesketh,[44,§] M. D. Hildreth,[54] R. Hirosky,[79] T. Hoang,[47] J. D. Hobbs,[70] B. Hoeneisen,[12] M. Hohlfeld,[24] Z. Hubacek,[10,18] N. Huske,[17] V. Hynek,[10] I. Iashvili,[67] Y. Ilchenko,[77] R. Illingworth,[48] A. S. Ito,[48] S. Jabeen,[75] M. Jaffré,[16] D. Jamin,[15] A. Jayasinghe,[73] R. Jesik,[43] K. Johns,[45] M. Johnson,[48] D. Johnston,[64] A. Jonckheere,[48] P. Jonsson,[43] J. Joshi,[27] A. W. Jung,[48] A. Juste,[40] K. Kaadze,[57] E. Kajfasz,[15] D. Karmanov,[37] P. A. Kasper,[48] I. Katsanos,[64] R. Kehoe,[77] S. Kermiche,[15] N. Khalatyan,[48] A. Khanov,[74] A. Kharchilava,[67] Y. N. Kharzheev,[35] M. H. Kirby,[51] J. M. Kohli,[27] A. V. Kozelov,[38] J. Kraus,[62] S. Kulikov,[38] A. Kumar,[67] A. Kupco,[11] T. Kurča,[20] V. A. Kuzmin,[37] J. Kvita,[9] S. Lammers,[52] G. Landsberg,[75] P. Lebrun,[20] H. S. Lee,[31] S. W. Lee,[55] W. M. Lee,[48] J. Lellouch,[17] L. Li,[46] Q. Z. Li,[48] S. M. Lietti,[5] J. K. Lim,[31] D. Lincoln,[48] J. Linnemann,[62] V. V. Lipaev,[38] R. Lipton,[48] Y. Liu,[7] Z. Liu,[6] A. Lobodenko,[39] M. Lokajicek,[11] R. Lopes de Sa,[70] H. J. Lubatti,[80] R. Luna-Garcia,[32,‖] A. L. Lyon,[48] A. K. A. Maciel,[2] D. Mackin,[78] R. Madar,[18] R. Magaña-Villalba,[32] S. Malik,[64] V. L. Malyshev,[35] Y. Maravin,[57] J. Martínez-Ortega,[32] R. McCarthy,[70] C. L. McGivern,[56] M. M. Meijer,[34] A. Melnitchouk,[63] D. Menezes,[50] P. G. Mercadante,[4] M. Merkin,[37] A. Meyer,[21] J. Meyer,[23] F. Miconi,[19] N. K. Mondal,[29] G. S. Muanza,[15] M. Mulhearn,[79] E. Nagy,[15] M. Naimuddin,[28] M. Narain,[75] R. Nayyar,[28] H. A. Neal,[61] J. P. Negret,[8] P. Neustroev,[39] S. F. Novaes,[5] T. Nunnemann,[25] G. Obrant,[39,††] J. Orduna,[78] N. Osman,[15] J. Osta,[54] G. J. Otero y Garzón,[1] M. Padilla,[46] A. Pal,[76] N. Parashar,[53] V. Parihar,[75] S. K. Park,[31] J. Parsons,[68] R. Partridge,[75,‡] N. Parua,[52] A. Patwa,[71] B. Penning,[48] M. Perfilov,[37] K. Peters,[44] Y. Peters,[44] K. Petridis,[44] G. Petrillo,[69] P. Pétroff,[16] R. Piegaia,[1] M.-A. Pleier,[71] P. L. M. Podesta-Lerma,[32,¶] V. M. Podstavkov,[48] P. Polozov,[36] A. V. Popov,[38] M. Prewitt,[78] D. Price,[52] N. Prokopenko,[38] S. Protopopescu,[71] J. Qian,[61] A. Quadt,[23] B. Quinn,[63] M. S. Rangel,[2] K. Ranjan,[28] P. N. Ratoff,[42] I. Razumov,[38] P. Renkel,[77] M. Rijssenbeek,[70] I. Ripp-Baudot,[19] F. Rizatdinova,[74] M. Rominsky,[48] A. Ross,[42] C. Royon,[18] P. Rubinov,[48] R. Ruchti,[54] G. Safronov,[36] G. Sajot,[14] P. Salcido,[50] A. Sánchez-Hernández,[32] M. P. Sanders,[25] B. Sanghi,[48] A. S. Santos,[5] G. Savage,[48] L. Sawyer,[58] T. Scanlon,[43] R. D. Schamberger,[70] Y. Scheglov,[39] H. Schellman,[51] T. Schliephake,[26] S. Schlobohm,[80] C. Schwanenberger,[44] R. Schwienhorst,[62] J. Sekaric,[56] H. Severini,[73] E. Shabalina,[23] V. Shary,[18] A. A. Shchukin,[38] R. K. Shivpuri,[28] V. Simak,[10] V. Sirotenko,[48] P. Skubic,[73] P. Slattery,[69] D. Smirnov,[54] K. J. Smith,[67] G. R. Snow,[64] J. Snow,[72] S. Snyder,[71] S. Söldner-Rembold,[44] L. Sonnenschein,[21] K. Soustruznik,[9] J. Stark,[14] V. Stolin,[36] D. A. Stoyanova,[38] M. Strauss,[73] D. Strom,[49] L. Stutte,[48] L. Suter,[44] P. Svoisky,[73] M. Takahashi,[44] A. Tanasijczuk,[1] W. Taylor,[6] M. Titov,[18] V. V. Tokmenin,[35] Y.-T. Tsai,[69] D. Tsybychev,[70] B. Tuchming,[18] C. Tully,[66] L. Uvarov,[39] S. Uvarov,[39] S. Uzunyan,[50] R. Van Kooten,[52] W. M. van Leeuwen,[33] N. Varelas,[49] E. W. Varnes,[45] I. A. Vasilyev,[38] P. Verdier,[20] L. S. Vertogradov,[35]

M. Verzocchi,[48] M. Vesterinen,[44] D. Vilanova,[18] P. Vokac,[10] H. D. Wahl,[47] M. H. L. S. Wang,[48] J. Warchol,[54] G. Watts,[80] M. Wayne,[54] M. Weber,[48,**] L. Welty-Rieger,[51] A. White,[76] D. Wicke,[26] M. R. J. Williams,[42] G. W. Wilson,[56] M. Wobisch,[58] D. R. Wood,[60] T. R. Wyatt,[44] Y. Xie,[48] C. Xu,[61] S. Yacoob,[51] R. Yamada,[48] W.-C. Yang,[44] T. Yasuda,[48] Y. A. Yatsunenko,[35] Z. Ye,[48] H. Yin,[48] K. Yip,[71] S. W. Youn,[48] J. Yu,[76] S. Zelitch,[79] T. Zhao,[80] B. Zhou,[61] J. Zhu,[61] M. Zielinski,[69] D. Zieminska,[52] and L. Zivkovic[75]

(The D0 Collaboration)

[1]*Universidad de Buenos Aires, Buenos Aires, Argentina*
[2]*LAFEX, Centro Brasileiro de Pesquisas Físicas, Rio de Janeiro, Brazil*
[3]*Universidade do Estado do Rio de Janeiro, Rio de Janeiro, Brazil*
[4]*Universidade Federal do ABC, Santo André, Brazil*
[5]*Instituto de Física Teórica, Universidade Estadual Paulista, São Paulo, Brazil*
[6]*Simon Fraser University, Vancouver, British Columbia, and York University, Toronto, Ontario, Canada*
[7]*University of Science and Technology of China, Hefei, People's Republic of China*
[8]*Universidad de los Andes, Bogotá, Colombia*
[9]*Charles University, Faculty of Mathematics and Physics, Center for Particle Physics, Prague, Czech Republic*
[10]*Czech Technical University in Prague, Prague, Czech Republic*
[11]*Center for Particle Physics, Institute of Physics, Academy of Sciences of the Czech Republic, Prague, Czech Republic*
[12]*Universidad San Francisco de Quito, Quito, Ecuador*
[13]*LPC, Université Blaise Pascal, CNRS/IN2P3, Clermont, France*
[14]*LPSC, Université Joseph Fourier Grenoble 1, CNRS/IN2P3, Institut National Polytechnique de Grenoble, Grenoble, France*
[15]*CPPM, Aix-Marseille Université, CNRS/IN2P3, Marseille, France*
[16]*LAL, Université Paris-Sud, CNRS/IN2P3, Orsay, France*
[17]*LPNHE, Universités Paris VI and VII, CNRS/IN2P3, Paris, France*
[18]*CEA, Irfu, SPP, Saclay, France*
[19]*IPHC, Université de Strasbourg, CNRS/IN2P3, Strasbourg, France*
[20]*IPNL, Université Lyon 1, CNRS/IN2P3, Villeurbanne, France and Université de Lyon, Lyon, France*
[21]*III. Physikalisches Institut A, RWTH Aachen University, Aachen, Germany*
[22]*Physikalisches Institut, Universität Freiburg, Freiburg, Germany*
[23]*II. Physikalisches Institut, Georg-August-Universität Göttingen, Göttingen, Germany*
[24]*Institut für Physik, Universität Mainz, Mainz, Germany*
[25]*Ludwig-Maximilians-Universität München, München, Germany*
[26]*Fachbereich Physik, Bergische Universität Wuppertal, Wuppertal, Germany*
[27]*Panjab University, Chandigarh, India*
[28]*Delhi University, Delhi, India*
[29]*Tata Institute of Fundamental Research, Mumbai, India*
[30]*University College Dublin, Dublin, Ireland*
[31]*Korea Detector Laboratory, Korea University, Seoul, Korea*
[32]*CINVESTAV, Mexico City, Mexico*
[33]*Nikhef, Science Park, Amsterdam, the Netherlands*
[34]*Radboud University Nijmegen, Nijmegen, the Netherlands and Nikhef, Science Park, Amsterdam, the Netherlands*
[35]*Joint Institute for Nuclear Research, Dubna, Russia*
[36]*Institute for Theoretical and Experimental Physics, Moscow, Russia*
[37]*Moscow State University, Moscow, Russia*
[38]*Institute for High Energy Physics, Protvino, Russia*
[39]*Petersburg Nuclear Physics Institute, St. Petersburg, Russia*
[40]*Institució Catalana de Recerca i Estudis Avançats (ICREA) and Institut de Física d'Altes Energies (IFAE), Barcelona, Spain*
[41]*Stockholm University, Stockholm and Uppsala University, Uppsala, Sweden*
[42]*Lancaster University, Lancaster LA1 4YB, United Kingdom*
[43]*Imperial College London, London SW7 2AZ, United Kingdom*
[44]*The University of Manchester, Manchester M13 9PL, United Kingdom*
[45]*University of Arizona, Tucson, Arizona 85721, USA*
[46]*University of California Riverside, Riverside, California 92521, USA*
[47]*Florida State University, Tallahassee, Florida 32306, USA*
[48]*Fermi National Accelerator Laboratory, Batavia, Illinois 60510, USA*
[49]*University of Illinois at Chicago, Chicago, Illinois 60607, USA*
[50]*Northern Illinois University, DeKalb, Illinois 60115, USA*
[51]*Northwestern University, Evanston, Illinois 60208, USA*

[52]Indiana University, Bloomington, Indiana 47405, USA
[53]Purdue University Calumet, Hammond, Indiana 46323, USA
[54]University of Notre Dame, Notre Dame, Indiana 46556, USA
[55]Iowa State University, Ames, Iowa 50011, USA
[56]University of Kansas, Lawrence, Kansas 66045, USA
[57]Kansas State University, Manhattan, Kansas 66506, USA
[58]Louisiana Tech University, Ruston, Louisiana 71272, USA
[59]Boston University, Boston, Massachusetts 02215, USA
[60]Northeastern University, Boston, Massachusetts 02115, USA
[61]University of Michigan, Ann Arbor, Michigan 48109, USA
[62]Michigan State University, East Lansing, Michigan 48824, USA
[63]University of Mississippi, University, Mississippi 38677, USA
[64]University of Nebraska, Lincoln, Nebraska 68588, USA
[65]Rutgers University, Piscataway, New Jersey 08855, USA
[66]Princeton University, Princeton, New Jersey 08544, USA
[67]State University of New York, Buffalo, New York 14260, USA
[68]Columbia University, New York, New York 10027, USA
[69]University of Rochester, Rochester, New York 14627, USA
[70]State University of New York, Stony Brook, New York 11794, USA
[71]Brookhaven National Laboratory, Upton, New York 11973, USA
[72]Langston University, Langston, Oklahoma 73050, USA
[73]University of Oklahoma, Norman, Oklahoma 73019, USA
[74]Oklahoma State University, Stillwater, Oklahoma 74078, USA
[75]Brown University, Providence, Rhode Island 02912, USA
[76]University of Texas, Arlington, Texas 76019, USA
[77]Southern Methodist University, Dallas, Texas 75275, USA
[78]Rice University, Houston, Texas 77005, USA
[79]University of Virginia, Charlottesville, Virginia 22901, USA
[80]University of Washington, Seattle, Washington 98195, USA

(Received 1 July 2011; published 16 September 2011)

We present an updated measurement of the anomalous like-sign dimuon charge asymmetry $A^b_{\rm sl}$ for semileptonic b-hadron decays in 9.0 fb^{-1} of $p\bar{p}$ collisions recorded with the D0 detector at a center-of-mass energy of $\sqrt{s} = 1.96$ TeV at the Fermilab Tevatron collider. We obtain $A^b_{\rm sl} = (-0.787 \pm 0.172(\text{stat}) \pm 0.093(\text{syst}))\%$. This result differs by 3.9 standard deviations from the prediction of the standard model and provides evidence for anomalously large CP violation in semileptonic neutral B decay. The dependence of the asymmetry on the muon impact parameter is consistent with the hypothesis that it originates from semileptonic b-hadron decays.

DOI: 10.1103/PhysRevD.84.052007 PACS numbers: 13.25.Hw, 11.30.Er, 14.40.Nd

I. INTRODUCTION

We measure the like-sign dimuon charge asymmetry of semileptonic decays of b hadrons

$$A^b_{\rm sl} \equiv \frac{N^{++}_b - N^{--}_b}{N^{++}_b + N^{--}_b}, \quad (1)$$

in 9.0 fb^{-1} of $p\bar{p}$ collisions recorded with the D0 detector at a center-of-mass energy $\sqrt{s} = 1.96$ TeV at the Fermilab Tevatron collider. Here N^{++}_b and N^{--}_b are the number of events containing two positively charged or two negatively charged muons, respectively, both of which are produced in prompt semileptonic b-hadron decays. At the Fermilab Tevatron $p\bar{p}$ collider, b quarks are produced mainly in $b\bar{b}$ pairs. Hence, to observe an event with two like-sign muons from semileptonic b-hadron decay, one of the hadrons must be a B^0 or B^0_s meson that oscillates and decays to a muon of charge opposite of that expected from the original b quark [1]. The oscillation $B^0_q \leftrightarrow \bar{B}^0_q$ ($q = d$ or s) is described by higher-order loop diagrams that are sensitive to hypothetical particles that may not be directly accessible at the Tevatron.

The asymmetry $A^b_{\rm sl}$ has contributions from the semileptonic charge asymmetries $a^d_{\rm sl}$ and $a^s_{\rm sl}$ of B^0 and B^0_s mesons [2], respectively

*Visitor from Augustana College, Sioux Falls, SD, USA.
†Visitor from The University of Liverpool, Liverpool, UK.
‡Visitor from SLAC, Menlo Park, CA, USA.
§Visitor from University College London, London, UK.
‖Visitor from Centro de Investigacion en Computacion - IPN, Mexico City, Mexico.
¶Visitor from ECFM, Universidad Autonoma de Sinaloa, Culiacán, Mexico.
**Visitor from Universität Bern, Bern, Switzerland.
††Deceased.

$$A_{\rm sl}^b = C_d a_{\rm sl}^d + C_s a_{\rm sl}^s, \tag{2}$$

$$\text{with } a_{\rm sl}^q = \frac{\Delta\Gamma_q}{\Delta M_q}\tan\phi_q, \tag{3}$$

where ϕ_q is a CP-violating phase, and ΔM_q and $\Delta\Gamma_q$ are the mass and width differences between the eigenstates of the propagation matrices of the neutral B_q^0 mesons. The coefficients C_d and C_s depend on the mean mixing probabilities and the production fractions of B^0 and B_s^0 mesons. We use the production fractions measured at LEP as averaged by the Heavy Flavor Averaging Group (HFAG) [3] and obtain

$$C_d = 0.594 \pm 0.022, \qquad C_s = 0.406 \pm 0.022. \tag{4}$$

The mean mixing probability measured by the CDF Collaboration recently [4] is consistent with the LEP value, which supports this choice of parameters. Using the standard model (SM) prediction for $a_{\rm sl}^d$ and $a_{\rm sl}^s$ [5], we find

$$A_{\rm sl}^b({\rm SM}) = (-0.028^{+0.005}_{-0.006})\%, \tag{5}$$

which is negligible compared to present experimental sensitivity. Additional contributions to CP violation via loop diagrams appear in some extensions of the SM and can result in an asymmetry $A_{\rm sl}^b$ within experimental reach [6–10].

This article is an update to Ref. [11] that reported evidence for an anomalous like-sign dimuon charge asymmetry with 6.1 fb^{-1} of data, at the 3.2 standard deviation level. All notations used here are given in Ref. [11]. This new measurement is based on a larger data set and further improvements in the measurement technique. In addition, the asymmetry's dependence on the muon impact parameter (IP) [12] is studied. The D0 detector is described in Ref. [13]. We include a brief overview of the analysis in Sec. II. Improvements made to muon selections are presented in Sec. III; the measurement of all quantities required to determine the asymmetry $A_{\rm sl}^b$ is described in Secs. IV, V, VI, VII, VIII, IX, and X, and the result is given in Sec. XI. Sections XII and XIII present consistency checks of the measurement; Sec. XIV describes the study of the asymmetry's IP dependence. Conclusions are given in Sec. XV.

II. METHOD

The elements of our analysis are described in detail in Ref. [11]. Here, we summarize briefly the method, emphasizing the improvements to our previous procedure. We use two sets of data: (i) *inclusive-muon* data collected with single muon triggers that provide n^+ positively charged muons and n^- negatively charged muons, and (ii) *like-sign dimuon* data, collected with dimuon triggers that provide N^{++} events with two positively charged muons and N^{--} events with two negatively charged muons. If an event contains more than one muon, each muon is included in the inclusive-muon sample. Such events constitute about 0.5% of the total inclusive-muon sample. If an event contains more than two muons, the two muons with the highest transverse momentum (p_T) are selected for inclusion in the dimuon sample. Such events make up about 0.7% of the total like-sign dimuon sample.

From these data we obtain the inclusive-muon charge asymmetry a and the like-sign dimuon charge asymmetry A, defined as

$$a = \frac{n^+ - n^-}{n^+ + n^-}, \qquad A = \frac{N^{++} - N^{--}}{N^{++} + N^{--}}. \tag{6}$$

In addition to a possible signal asymmetry $A_{\rm sl}^b$, these asymmetries have contributions from muons produced in kaon and pion decay, or from hadrons that punch through the calorimeter and iron toroids to penetrate the outer muon detector. The charge asymmetry related to muon detection and identification also contributes to a and A. These contributions are measured with data, with only minimal input from simulation. The largest contribution by far is from kaon decays. Positively charged kaons have smaller cross sections in the detector material than negatively charged kaons [14], giving them more time to decay. This difference produces a positive charge asymmetry.

We consider muon candidates with p_T in the range 1.5 to 25 GeV. This range is divided into six bins as shown in Table I. The inclusive-muon charge asymmetry a can be expressed [11] as

$$a = \sum_{i=1}^{6} f_\mu^i \{ f_S^i (a_S + \delta_i) + f_K^i a_K^i + f_\pi^i a_\pi^i + f_p^i a_p^i \}, \tag{7}$$

where the fraction of reconstructed muons, f_μ^i, in a given p_T interval i in the inclusive-muon sample is given in Table I. The fractions of these muons produced by kaons, pions, and protons in a given p_T interval i are f_K^i, f_π^i, and f_p^i, and their charge asymmetries are a_K^i, a_π^i, and a_p^i, respectively. We refer to these muons as "long" or "L" muons since they are produced by particles traveling long distances before decaying within the detector material. The track of a L muon in the central tracker is dominantly produced by the parent hadron. The charge asymmetry of L muons results from the difference in the interactions of positively and negatively charged particles with the

TABLE I. Fractions of muon candidates in the inclusive-muon sample (f_μ^i) and in the like-sign dimuon sample (F_μ^i, with two entries per event).

Bin	Muon p_T range (GeV)	f_μ^i	F_μ^i
1	1.5–2.5	0.0077	0.0774
2	2.5–4.2	0.2300	0.3227
3	4.2–5.6	0.4390	0.3074
4	5.6–7.0	0.1702	0.1419
5	7.0–10.0	0.1047	0.1057
6	10.0–25.0	0.0484	0.0449

detector material, and is not related to CP violation. The background fraction is defined as $f^i_{\rm bkg} = f^i_K + f^i_\pi + f^i_p$. The quantity $f^i_S = 1 - f^i_{\rm bkg}$ is the fraction of muons from weak decays of b and c quarks and τ leptons, and from decays of short-lived mesons (ϕ, ω, η, ρ^0). We refer to these muons as "short" or "S" muons, since they arise from the decay of particles at small distances from the $p\bar{p}$ interaction point. These particles are not affected by interactions in the detector material, and once muon detection and identification imbalances are removed, the muon charge asymmetry a_S must therefore be produced only through CP violation in the underlying physical processes. The quantity δ_i in Eq. (7) is the charge asymmetry related to muon detection and identification. The background charge asymmetries a^i_K, a^i_π, and a^i_p are measured in the inclusive-muon data, and include any detector asymmetry. The δ_i therefore accounts only for S muons and is multiplied by the factor f^i_S.

The like-sign dimuon charge asymmetry A can be expressed [11] as

$$A = F_{SS}A_S + F_{SL}a_S + \sum_{i=1}^{6} F^i_\mu\{(2 - F^i_{\rm bkg})\delta_i + F^i_K a^i_K + F^i_\pi a^i_\pi + F^i_p a^i_p\}. \quad (8)$$

The quantity A_S is the charge asymmetry of the events with two like-sign S muons. The quantity F_{SS} is the fraction of like-sign dimuon events with two S muons, F_{SL} is the fraction of like-sign dimuon events with one S and one L muon. We also define the quantity F_{LL} as the fraction of like-sign dimuon events with two L muons. The quantity F^i_μ is the fraction of muons in the p_T interval i in the like-sign dimuon data. The quantities F^i_x ($x = K,\ \pi,\ p$) are defined as $F^i_x \equiv 2N^i_x/N^i_\mu$, where N^i_x is the number of muons produced by kaons, pions, and protons, respectively, in a p_T interval i, with N^i_μ being the number of muons in this interval, with the factor of 2 taking into account the normalization of these quantities per like-sign dimuon event. The quantity $F^i_{\rm bkg}$ is a sum over muons produced by hadrons

$$F^i_{\rm bkg} \equiv F^i_K + F^i_\pi + F^i_p. \quad (9)$$

We also define $F_{\rm bkg}$ as

$$F_{\rm bkg} \equiv \sum_{i=1}^{6}(F^i_\mu F^i_{\rm bkg}) \quad (10)$$

$$= F_{SL} + 2F_{LL} = 1 + F_{LL} - F_{SS}. \quad (11)$$

The estimated contribution from the neglected quadratic terms in Eq. (8) is approximately 2×10^{-5}, which corresponds to about 5% of the statistical uncertainty on A.

The asymmetries a_S and A_S in Eqs. (7) and (8) are the only asymmetries due to CP violation in the processes producing S muons, and are proportional to the asymmetry $A^b_{\rm sl}$

$$a_S = c_b A^b_{\rm sl}, \qquad A_S = C_b A^b_{\rm sl}. \quad (12)$$

The dilution coefficients c_b and C_b are discussed in Ref. [11] and in Sec. X below.

Equations (7)–(12) are used to measure the asymmetry $A^b_{\rm sl}$. The major contributions to the uncertainties on $A^b_{\rm sl}$ are from the statistical uncertainty on A and the total uncertainty on F^i_K, f^i_K and δ_i. To reduce the latter contributions, we measure the asymmetry $A^b_{\rm sl}$ using the asymmetry A', which is defined as

$$A' \equiv A - \alpha a. \quad (13)$$

Since the same physical processes contribute to both F^i_K and f^i_K, their uncertainties are strongly correlated, and therefore partially cancel in Eq. (13) for an appropriate choice of the coefficient α. The contribution from the asymmetry $A^b_{\rm sl}$, however, does not cancel in Eq. (13) because $c_b \ll C_b$ [11]. Full details of the measurements of different quantities entering in Eqs. (7)–(12) are given in Ref. [11]. The main improvements in the present analysis are related to muon selection and the measurement of F^i_K and f^i_K. These modifications are described in Sections III, IV, and V.

III. MUON SELECTION

The muon selection is similar to that described in Ref. [11]. The inclusive-muon and like-sign dimuon samples are obtained from data collected with single and dimuon triggers, respectively. Charged particles with transverse momentum in the range $1.5 < p_T < 25$ GeV and with pseudorapidity $|\eta| < 2.2$ [15] are considered as muon candidates. The upper limit on p_T is applied to suppress the contribution of muons from W and Z boson decays. To ensure that the muon candidate passes through the detector, including all three layers of the muon system, we require either $p_T > 4.2$ GeV or a longitudinal momentum component $|p_z| > 5.4$ GeV. Muon candidates are selected by matching central tracks with a segment reconstructed in the muon system and by applying tight quality requirements aimed at reducing false matching and background from cosmic rays and beam halo. The transverse impact parameter of the muon track relative to the reconstructed $p\bar{p}$ interaction vertex must be smaller than 0.3 cm, with the longitudinal distance from the point of closest approach to this vertex smaller than 0.5 cm. Strict quality requirements are also applied to the tracks and to the reconstructed $p\bar{p}$ interaction vertex. The inclusive-muon sample contains all muons passing the selection requirements. If an event contains more than one muon, each muon is included in the inclusive-muon sample. The like-sign dimuon sample contains all events with at least two muon candidates with the same charge. These two muons are required to have an invariant mass greater than 2.8 GeV

to minimize the number of events in which both muons originate from the same b quark (e.g., $b \to \mu$, $b \to c \to \mu$). Compared to Ref. [11], the following modifications to the muon selection are applied:

(i) To reduce background from a mismatch of tracks in the central detector with segments in the outer muon system, we require that the sign of the curvature of the track measured in the central tracker be the same as in the muon system. This selection was not applied in Ref. [11], and removes only about 1% of the dimuon events.

(ii) To ensure that the muon candidate can penetrate all three layers of the muon detector, we require either a transverse momentum $p_T > 4.2$ GeV, or a longitudinal momentum component $|p_z| > 5.4$ GeV, instead of $p_T > 4.2$ GeV or $|p_z| > 6.4$ GeV in Ref. [11]. With this change, the number of like-sign dimuon events increases by 25%, without impacting the condition that the muon must penetrate the calorimeter and toroids, as can be deduced from Fig. 1.

(iii) To reduce background from kaon and pion decays in flight, we require that the χ^2 calculated from the difference between the track parameters measured in the central tracker and in the muon system be $\chi^2 < 12$ (for 4 d.o.f.) instead of 40 used in Ref. [11]. With this tighter selection, the number of like-sign dimuon events is decreased by 12%.

Compared to the selections applied in Ref. [11], the total number of like-sign dimuon events after applying all these modifications is increased by 13% in addition to the increase due to the larger integrated luminosity of this analysis.

The muon charge is determined by the central tracker. The probability of charge mismeasurement is obtained by comparing the charge measured by the central tracker and by the muon system and is found to be less than 0.1%.

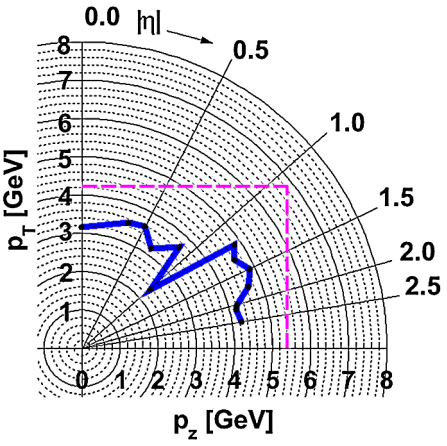

FIG. 1 (color online). Smallest muon momentum required to penetrate the calorimeter and toroids at different pseudorapidities, $|\eta|$ (solid line), and the momentum selection used in this analysis (dashed line).

TABLE II. Weights assigned to the events recorded with different solenoid and toroid polarities in the inclusive-muon and like-sign dimuon samples.

Solenoid polarity	Toroid polarity	Weight inclusive-muon	Weight like-sign dimuon
−1	−1	0.994	0.964
−1	+1	1.000	1.000
+1	−1	0.985	0.958
+1	+1	0.989	0.978

The polarities of the toroidal and solenoidal magnets are reversed on average every two weeks so that the four solenoid-toroid polarity combinations are exposed to approximately the same integrated luminosity. This allows for a cancellation of first-order effects related to the instrumental asymmetry [16]. To ensure such cancellation, the events are weighted according to the number of events for each data sample corresponding to a different configuration of the magnets' polarities. These weights are given in Table II. During the data taking of the last part of the sample, corresponding to approximately 2.9 fb^{-1} of $p\bar{p}$ collisions, the magnet polarities were specially chosen to equalize the number of dimuon events with different polarities in the entire sample. The weights in Table II are therefore closer to unity compared to those used in Ref. [11].

IV. MEASUREMENT OF f_K, f_π, f_p

The fraction f_K^i in the inclusive-muon sample is measured using $K^{*0} \to K^+\pi^-$ decays, with the kaon identified as a muon (see Ref. [11] for details). The transverse momentum of the K^+ meson is required to be in the p_T interval i. Since the momentum of a particle is measured by the central tracking detector, a muon produced by a kaon is assigned the momentum of this kaon (a small correction for kaons decaying within the tracker volume is introduced later). The fraction $f_{K^{*0}}^i$ of these decays is converted to the fraction f_K^i using the relation

$$f_K^i = \frac{n_i(K_S^0)}{n_i(K^{*+} \to K_S^0\pi^+)} f_{K^{*0}}^i, \tag{14}$$

where $n_i(K_S^0)$ and $n_i(K^{*+} \to K_S^0\pi^+)$ are the number of reconstructed $K_S^0 \to \pi^+\pi^-$ and $K^{*+} \to K_S^0\pi^+$ decays, respectively. The transverse momentum of the K_S^0 meson is required to be in the p_T interval i. We require in addition that one of the pions from the $K_S^0 \to \pi^+\pi^-$ decay be identified as a muon. In the previous analysis [11] the production of K^{*+} mesons was studied in a sample of events with an additional reconstructed muon, but we did not require that this muon be associated with a pion from

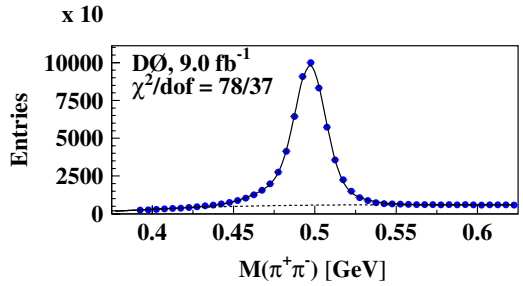

FIG. 2 (color online). The $\pi^+\pi^-$ invariant mass distribution for K^0_S candidates in the inclusive-muon sample with at least one pion identified as a muon with $4.2 < p_T(K^0_S) < 5.6$ GeV. The solid line represents the result of the fit to the K^0_S content, and the dashed line represents the fitted background contribution.

$K^0_S \to \pi^+\pi^-$ decay. The fraction of events containing b and/or c quarks was therefore enhanced in the sample, which could result in a bias of the measured fraction f_K. This bias does not exceed the systematic uncertainty of f_K and its impact on the $A^b_{\rm sl}$ value is less than 0.03%. The application of the new requirement ensures that the flavor composition in the selected $K^{*+} \to K^0_S\pi^+$ and $K^{*0} \to K^+\pi^-$ samples is the same and this bias is eliminated.

The selection criteria and fitting procedures used to select and determine the number of K^0_S, K^{*+} and K^{*0} events are given in Ref. [11]. As an example, Fig. 2 displays the $\pi^+\pi^-$ invariant mass distribution and the fitted $K^0_S \to \pi^+\pi^-$ candidates in the inclusive-muon sample, with at least one pion identified as a muon, for $4.2 < p_T(K^0_S) < 5.6$ GeV. Figure 3 shows the $K^0_S\pi^+$ mass distribution and fit to $K^{*+} \to K^0_S\pi^+$ candidates for all K^0_S candidates with $4.2 < p_T(K^0_S) < 5.6$ GeV and $480 < M(\pi^+\pi^-) < 515$ MeV. Figure 4 shows the $K^+\pi^-$ mass distribution and the fit result for $K^{*0} \to K^+\pi^-$ candidates for all kaons with $4.2 < p_T(K^+) < 5.6$ GeV. The $K^+\pi^-$ mass distribution contains contributions from light meson resonances decaying to $\pi^+\pi^-$. The most important contribution comes from the $\rho^0 \to \pi^+\pi^-$ decay with $\pi \to \mu$. It produces a broad peak in the mass region close to the K^{*0} mass. The distortions in the background distribution due to other light resonances, which are not identified explicitly, can also be seen in Fig. 4. Our background model therefore includes the contribution of $\rho^0 \to \pi^+\pi^-$ and two additional Gaussian terms to take into account the distortions around 1.1 GeV. More details of the background description are given in Ref. [11].

The measurement of the fractions f_π and f_p is also performed using the method of Ref. [11]. The values of f_K and f_π are divided by the factors C_K and C_π, respectively, which take into account the fraction of kaons and pions reconstructed by the tracking system before they decay. These factors are discussed in Ref. [11], and are determined through simulation. Contrary to Ref. [11], this analysis determines these factors separately for kaons and pions. We find the values

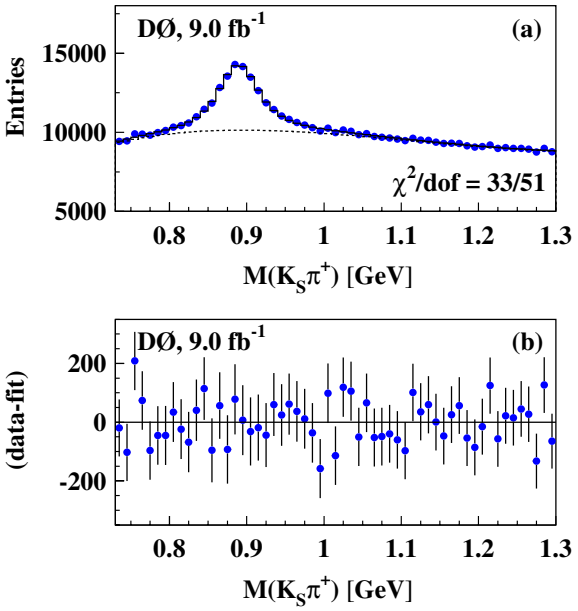

FIG. 3 (color online). (a) The $K^0_S\pi^+$ invariant mass distribution for K^{*+} candidates in the inclusive-muon sample. The K^0_S candidate is required to have $480 < M(\pi^+\pi^-) < 515$ MeV and $4.2 < p_T(K^0_S) < 5.6$ GeV. The solid line represents the result of the fit to the K^{*+} content, and the dashed line shows the background contribution. (b) Difference between data and the result of the fit.

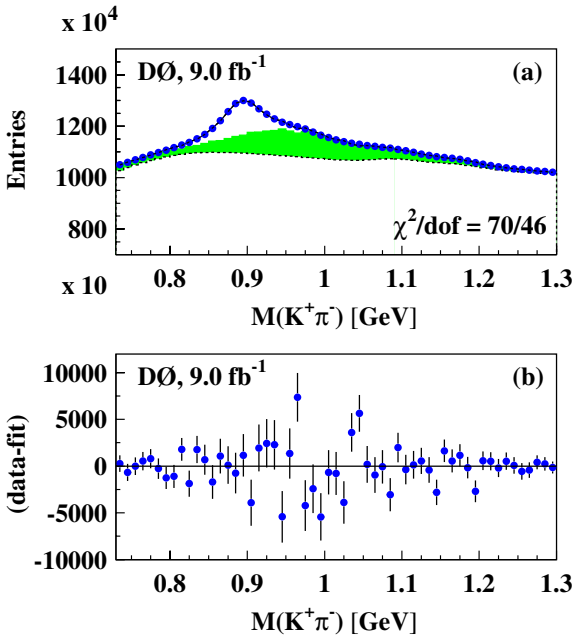

FIG. 4 (color online). (a) The $K^+\pi^-$ invariant mass distribution for K^{*0} candidates in the inclusive-muon sample for all kaons with $4.2 < p_T(K^+) < 5.6$ GeV. The solid line corresponds to the result of the fit to the K^{*0} content, and the dashed line shows the contribution from combinatorial background. The shaded histogram is the contribution from $\rho^0 \to \pi^+\pi^-$ events. (b) Difference between data and the result of the fit.

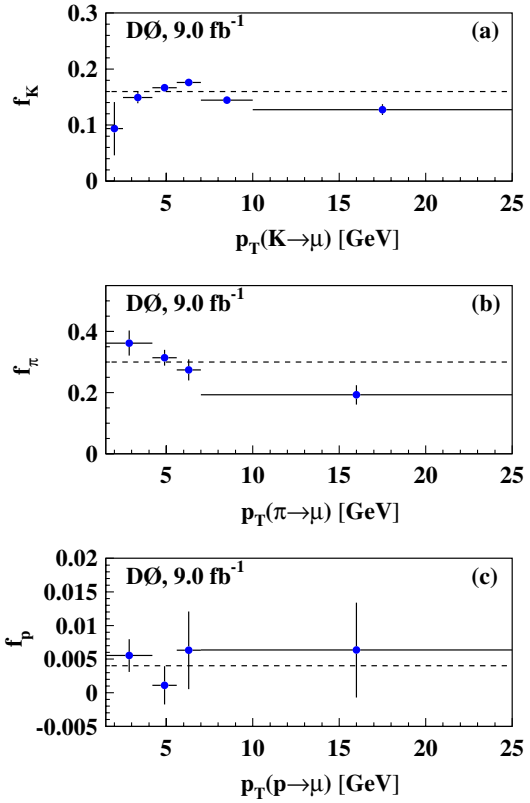

FIG. 5 (color online). The fraction of (a) $K \to \mu$ tracks, (b) $\pi \to \mu$ tracks and (c) $p \to \mu$ tracks in the inclusive-muon sample as a function of the kaon, pion and proton p_T, respectively. The horizontal dashed lines show the mean values.

$$C_K = 0.920 \pm 0.006, \qquad C_\pi = 0.932 \pm 0.006. \quad (15)$$

The uncertainties include contributions from the number of simulated events and from the uncertainties in the momentum spectrum of the generated particles.

The values of f_K, f_π and f_p in different muon p_T bins are shown in Fig. 5 and in Table III. The changes in the muon candidates selection adopted here is the main source of differences relative to the corresponding values in Ref. [11]. The fractions f_π and f_p are poorly measured in bins 1 and 2, and bins 5 and 6, due to the small number of events, and their contents are therefore combined through their weighted average.

TABLE III. Fractions f_K, f_π, and f_p for different p_T bins. The bottom row shows the weighted average of these quantities obtained with weights given by the fraction of muons in a given p_T interval, f_μ^i, in the inclusive-muon sample, see Table I. Only statistical uncertainties are given.

Bin	$f_K \times 10^2$	$f_\pi \times 10^2$	$f_p \times 10^2$
1	9.35 ± 4.77	36.20 ± 4.12	0.55 ± 0.24
2	14.91 ± 1.00		
3	16.65 ± 0.41	31.42 ± 2.57	0.11 ± 0.29
4	17.60 ± 0.49	27.41 ± 3.46	0.63 ± 0.58
5	14.43 ± 0.45	19.25 ± 3.19	0.64 ± 0.71
6	12.75 ± 0.97		
All	15.96 ± 0.24	30.01 ± 1.60	0.38 ± 0.17

V. MEASUREMENT OF F_K, F_π, F_p

The quantity F_K is expressed as

$$F_K = R_K f_K, \quad (16)$$

where R_K is the ratio of the fractions of muons produced by kaons in like-sign dimuon and in inclusive-muon data. For the p_T interval i, R_K is defined as

$$R_{K,i} = 2\frac{N_i(K \to \mu)}{n_i(K \to \mu)}\frac{n_i(\mu)}{N_i(\mu)}, \quad (17)$$

where $N_i(K \to \mu)$ and $n_i(K \to \mu)$ are the number of reconstructed K mesons identified as muons in the like-sign dimuon and in the inclusive-muon samples, respectively. The transverse momentum of the K meson is required to be in the p_T interval i. The quantities $N_i(\mu)$ and $n_i(\mu)$ are the number of muons in the p_T interval i. A multiplicative factor of 2 is included in Eq. (17) because there are two muons in a like-sign dimuon event, and F_K is normalized to the number of like-sign dimuon events.

In the previous analysis [11], the quantity F_K was obtained from a measurement of the K^{*0} production rate. Presenting it in the form of Eq. (16) also allows the determination of F_K through an independent measurement of the fraction of K_S^0 mesons in dimuon and in inclusive-muon data where one of the pions from $K_S^0 \to \pi^+\pi^-$ decay is identified as a muon. This measurement is discussed below. In addition, Eq. (16) offers an explicit separation of systematic uncertainties associated with F_K. The systematic uncertainty on the fraction f_K affects the two determinations of $A_{\rm sl}^b$ based on Eqs. (7) and (8) in a fully correlated way; therefore, its impact on the measurement obtained using Eq. (13) is significantly reduced. The systematic uncertainty on the ratio R_K does not cancel in Eq. (13). It is estimated directly from a comparison of the values of R_K obtained in two independent channels.

One way to measure R_K is from the fraction of $K^{*0} \to K^+\pi^-$ events in the inclusive-muon and like-sign dimuon data

$$R_{K,i}(K^{*0}) = 2\frac{N_i(K^{*0} \to \mu)}{n_i(K^{*0} \to \mu)}\frac{n_i(\mu)}{N_i(\mu)}, \quad (18)$$

where $N_i(K^{*0} \to \mu)$ and $n_i(K^{*0} \to \mu)$ are the number of reconstructed $K^{*0} \to K^+\pi^-$ decays, with the kaon identified as a muon in the like-sign dimuon and in the inclusive-muon samples, respectively. The transverse momentum of the K meson is required to be in the p_T interval i. The measurement using Eq. (18) is based on the assumption

$$\frac{N_i(K^{*0} \to \mu)}{n_i(K^{*0} \to \mu)} = \frac{N_i(K \to \mu)}{n_i(K \to \mu)}, \tag{19}$$

which was validated through simulations in Ref. [11]. The corresponding systematic uncertainty is discussed below.

In Ref. [11], the fractions $F_{K^{*0}}$ and $f_{K^{*0}}$ were obtained independently from a fit of the $K^+\pi^-$ invariant mass distribution in the like-sign dimuon and inclusive-muon sample, respectively. Figure 6 shows the same mass studies as in Fig. 4, but for the like-sign dimuon sample. The fit in both cases is complicated by the contribution from light meson resonances that decay to $\pi^+\pi^-$, producing a reflection in the $K^+\pi^-$ invariant mass distribution. In addition, the detector resolution is not known *a priori* and has to be included in the fit. All these complications are reduced significantly or eliminated in the ''null-fit'' method introduced in Ref. [11], which is used in this analysis to measure the ratio $R_K(K^{*0})$.

In this method, for each p_T interval i, we define a set of distributions $P_i(M_{K\pi};\xi)$ that depend on a parameter ξ

$$P_i(M_{K\pi};\xi) = N_i(M_{K\pi}) - \xi\frac{N_i(\mu)}{2n_i(\mu)}n_i(M_{K\pi}), \tag{20}$$

where $N_i(M_{K\pi})$ and $n_i(M_{K\pi})$ are the number of entries in the p_T bin i of the $K^+\pi^-$ invariant mass distributions in the like-sign dimuon and inclusive-muon samples, respectively. For each value of ξ the number of $K^{*0} \to K^+\pi^-$ decays, $\mathcal{N}(K^{*0})$, and its uncertainty, $\Delta\mathcal{N}(K^{*0})$, are measured from the $P_i(M_{K\pi};\xi)$ distribution. The value of ξ for which $\mathcal{N}(K^{*0}) = 0$ defines $R_{K,i}(K^{*0})$. The uncertainty $\sigma(R_{K,i})$ is determined from the condition that $\mathcal{N}(K^{*0}) = \pm\Delta\mathcal{N}(K^{*0})$ corresponding to $\xi = R_{K,i}(K^{*0}) \pm \sigma(R_{K,i})$.

The advantage of this method is that the influence of the detector resolution becomes minimal for $\mathcal{N}(K^{*0})$ close to zero, and the contribution from the peaking background is reduced in $P_i(M_{K\pi};\xi)$ to the same extent as the contribution of K^{*0} mesons, and becomes negligible when $\mathcal{N}(K^{*0})$ is close to zero. As an example, Fig. 7 shows the mass distribution $P_i(M_{K\pi};\xi)$ for $\xi = 0.88$, for all kaons with $4.2 < p_T(K^+) < 5.6$ GeV. This distribution is obtained from the distributions shown in Figs. 4 and 6, using Eq. (20). The contributions of both $K^{*0} \to K^+\pi^-$ and $\rho^0 \to \pi^+\pi^-$, as well as any other resonance in the background, disappear. As a result, the fitting procedure becomes more robust, the fitting range can be extended, and the resulting value of $R_K(K^{*0})$ becomes stable under a variation of the fitting parameters over a wider range.

The value of R_K is also obtained from the production rate of K^0_S mesons in the inclusive-muon and dimuon samples. We compute $R_{K,i}$ for a given p_T interval i as

$$R_{K,i}(K^0_S) = \frac{N_i(K^0_S \to \mu)}{n_i(K^0_S \to \mu)}\frac{n_i(\mu)}{N_i(\mu)}\kappa_i, \tag{21}$$

where $N_i(K^0_S \to \mu)$ and $n_i(K^0_S \to \mu)$ are the number of reconstructed $K^0_S \to \pi^+\pi^-$ decays with one pion identified as a muon in the dimuon and the inclusive-muon data, respectively. The correction factor κ_i is discussed later in this section. The measurement of $R_{K,i}$ using Eq. (21) assumes isospin invariance and consequent equality of the ratio of production rates in the dimuon and in the inclusive-muon samples of K^+ and K^0_S mesons, i.e.,

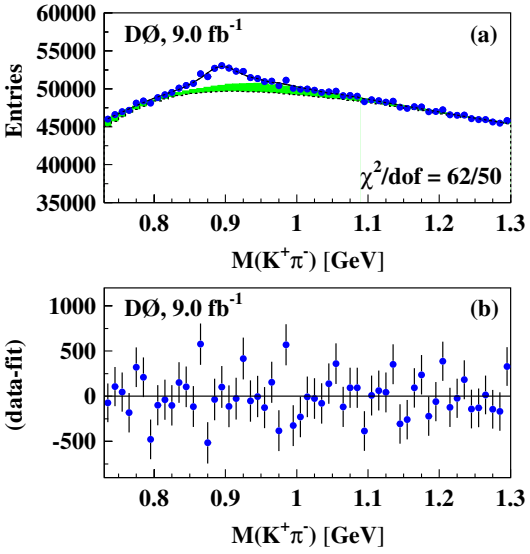

FIG. 6 (color online). (a) The $K^+\pi^-$ invariant mass distribution of K^{*0} candidates in the like-sign dimuon sample for all kaons with $4.2 < p_T(K^+) < 5.6$ GeV. The solid line corresponds to the result of the fit to the K^{*0} content, and the dashed line shows the contribution from combinatorial background. The shaded histogram is the contribution from $\rho^0 \to \pi^+\pi^-$ events. (b) Difference between data and the result of the fit.

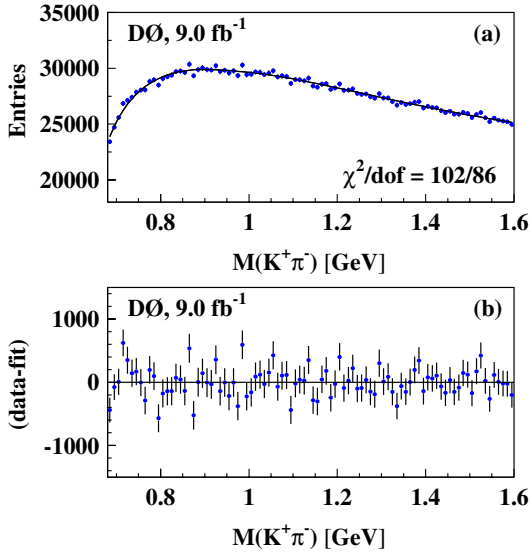

FIG. 7 (color online). (a) The $K^+\pi^-$ invariant mass distribution $P_2(M_{K\pi};\xi)$ obtained using Eq. (20) for $\xi = 0.88$ for all kaons with $4.2 < p_T(K^+) < 5.6$ GeV. The dashed line shows the contribution from the combinatorial background. (b) Difference between data and the result of the fit.

$$\frac{N_i(K_S^0 \to \mu)}{n_i(K_S^0 \to \mu)} = \frac{N_i(K \to \mu)}{n_i(K \to \mu)}. \quad (22)$$

Since the charged kaon p_T in Eq. (22) is required to be within the p_T interval i, the transverse momentum of the K_S^0 meson in Eq. (21) is also required to be within the p_T interval i. We expect approximately the same number of positive and negative pions from $K_S^0 \to \pi^+\pi^-$ decays to be identified as a muon. Therefore, we use both like-sign and opposite-sign dimuon events to measure $N_i(K_S^0 \to \mu)$ and we do not use the multiplicative factor of 2 in Eq. (21). The requirement of having one pion identified as a muon makes the flavor composition in the samples of charged $K \to \mu$ events and $K_S^0 \to \mu$ events similar.

The charges of the kaon and the additional muon in a dimuon event can be correlated, i.e., in general $N(K^+\mu^+) \neq N(K^-\mu^+)$. However, the number of $N_i(K_S^0 \to \mu)$ events is not correlated with the charge of the additional muon, i.e., $N(K_S^0 \to \mu^+, \mu^+) = N(K_S^0 \to \mu^-, \mu^+)$. Since the ratio $R_{K,i}$ is determined for the sample of like-sign dimuon events, we apply in Eq. (21) the correction factor κ_i, defined as

$$\kappa_i \equiv \frac{2(N(K^+\mu^+) + \text{c.c.})}{(N(K^+\mu^+) + N(K^-\mu^+) + \text{c.c.})}, \quad (23)$$

to take into account the correlation between the charges of the kaon and muon. The abbreviation "c.c." in Eq. (23) denotes "charge conjugate states". The coefficients κ_i are measured in data using the events with a reconstructed $K^{*0} \to K^+\pi^-$ decay and an additional muon. To reproduce the selection for the dimuon sample [11], the invariant mass of the $K\mu$ system, with the kaon assigned the mass of a muon, is required to be greater than 2.8 GeV. The fitting procedure and selection criteria to measure the number of K^{*0} events are described in Ref. [11]. The values of κ_i for different p_T intervals are given in Fig. 8 and in Table IV.

The average muon detection efficiency is different for the inclusive-muon and like-sign dimuon samples because of different p_T thresholds used in their triggers. The difference in muon detection efficiency is large for muons with small p_T, but it is insignificant for muons above the inclusive-muon trigger threshold. The ratio $N_i(K_S^0 \to \mu)/n_i(K_S^0 \to \mu)$ in Eq. (21) is measured as a function of the transverse momenta of K_S^0 mesons, $p_T(K_S^0)$, while the ratio $n_i(\mu)/N_i(\mu)$ is measured in bins of muon p_T. Each $p_T(K_S^0)$ bin contains $\pi \to \mu$ with different $p_T(\pi \to \mu)$ values. The muon detection efficiency therefore does not cancel in Eq. (21), and can affect the measurement of $R_K(K_S^0)$. Figure 9 shows the ratio of $\pi \to \mu$ detection efficiencies in the inclusive-muon and dimuon data. To compute this ratio, we select the K_S^0 mesons in a given $p_T(K_S^0)$ interval. The $p_T(\pi)$ distribution of pions produced in the $K_S^0 \to \pi^+\pi^-$ decay with a given $p_T(K_S^0)$ is the same in the dimuon and inclusive-muon data. Therefore, any difference in this $p_T(\pi \to \mu)$ distribution between dimuon and inclusive-muon data is due to the $\pi \to \mu$ detection. We compute the ratio of these $p_T(\pi \to \mu)$ distributions, and normalize it such that it equals unity for $p_T(\pi \to \mu) > 5.6$ GeV. The value of this p_T threshold corresponds to the p_T threshold for single muon triggers. Figure 9 presents the average of the ratios for different $p_T(\mu)$ intervals. The ratio is suppressed for $p_T(\pi \to \mu) < 4.2$ GeV, and is consistent with a constant for $p_T(\pi \to \mu) > 4.2$ GeV. To remove the bias due to the trigger threshold, we measure $R_K(K_S^0)$ for events with $p_T(\pi \to \mu) > 4.2$ GeV. As a result, the ratio R_K is not defined for the first two p_T bins in the K_S^0 channel.

The values of $R_K(K^{*0})$ obtained through the null-fit method, for different muon p_T bins, are shown in Fig. 10(a) and in Table V. The values of $R_K(K_S^0)$ are contained in Fig. 10(b) and in Table V. The difference

TABLE IV. Values of κ in different p_T bins. The bottom row shows their average. Only statistical uncertainties are given.

bin	κ
1	1.005 ± 0.024
2	1.025 ± 0.016
3	1.038 ± 0.016
4	1.036 ± 0.016
5	1.051 ± 0.016
6	1.080 ± 0.013
Mean	1.046 ± 0.007

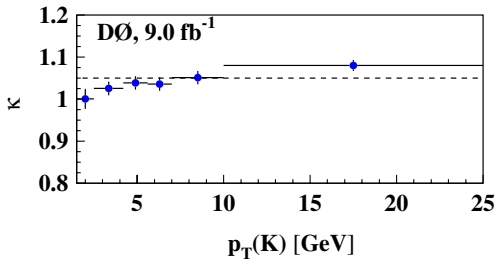

FIG. 8 (color online). The correction coefficient κ as a function of the kaon transverse momentum. The horizontal dashed line shows the mean value.

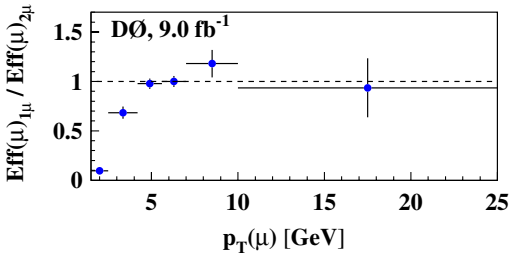

FIG. 9 (color online). The ratio of $\pi \to \mu$ detection efficiencies for the inclusive-muon and dimuon data as a function of the muon transverse momentum. The horizontal dashed line shows the mean value for $p_T(K) > 4.2$ GeV.

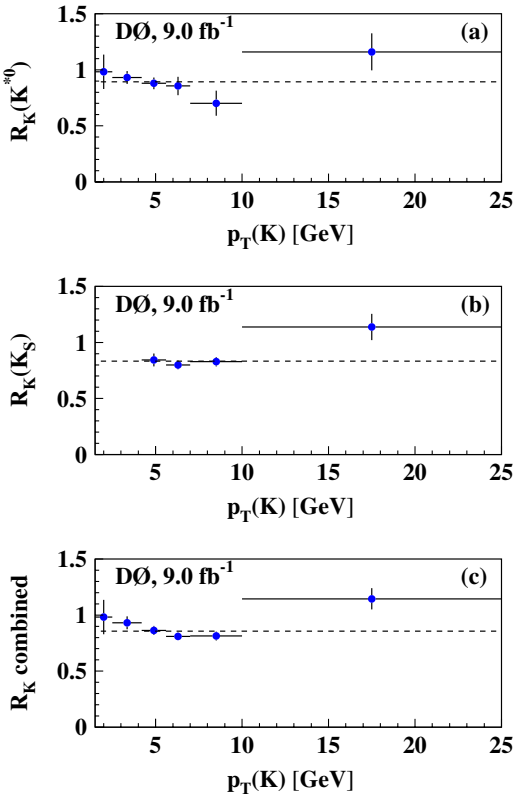

FIG. 10 (color online). The ratio R_K obtained using (a) K^{*0} production, (b) K^0_S production, and (c) combination of these two channels as a function of the kaon transverse momentum. The horizontal dashed lines show the mean values.

between the values of R_K measured with K^{*0} mesons and with K^0_S mesons is shown in Fig. 11. The mean value of this difference is

$$\Delta R_K = 0.01 \pm 0.05, \tag{24}$$

and the χ^2/d.o.f. is 1.7/4. We use two independent methods, each relying on different assumptions, to measure the ratio R_K and obtain results that are consistent with each other. The methods are subject to different systematic uncertainties, and therefore provide an important cross-check. As an independent cross-check, the value of R_K obtained in simulation is consistent with that measured in data; see Sec. XIII for details. We take the average of the two channels weighted by their uncertainties as our final values of R_K for $p_T(K) > 4.2$ GeV and use the values measured in the K^{*0} channel for $p_T(K) < 4.2$ GeV. These values are given in Table V and in Fig. 10(c). As we do not observe any difference between the two measurements, we take half of the uncertainty of ΔR_K as the systematic uncertainty of R_K. This corresponds to a relative uncertainty of 3.0% on the value of R_K. In our previous

TABLE V. Values of R_K obtained using K^{*0} and K^0_S meson production in different p_T bins. The bottom row shows their average. Only statistical uncertainties are given. The ratio R_K in the K^0_S channel is not measured in the first two bins, see Sec. V.

bin	R_K from K^{*0}	R_K from K^0_S	average R_K
1	0.983 ± 0.154		0.983 ± 0.154
2	0.931 ± 0.058		0.931 ± 0.058
3	0.880 ± 0.052	0.844 ± 0.059	0.864 ± 0.039
4	0.856 ± 0.082	0.800 ± 0.040	0.811 ± 0.036
5	0.702 ± 0.112	0.828 ± 0.042	0.813 ± 0.039
6	1.160 ± 0.165	1.138 ± 0.117	1.146 ± 0.095
Mean	0.892 ± 0.032	0.834 ± 0.025	0.856 ± 0.020

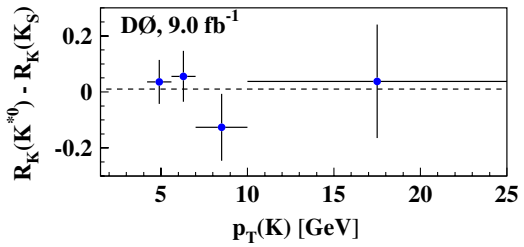

FIG. 11 (color online). The difference $R_K(K^{*0}) - R_K(K^0_S)$ as a function of kaon transverse momentum. The horizontal dashed line shows the mean value.

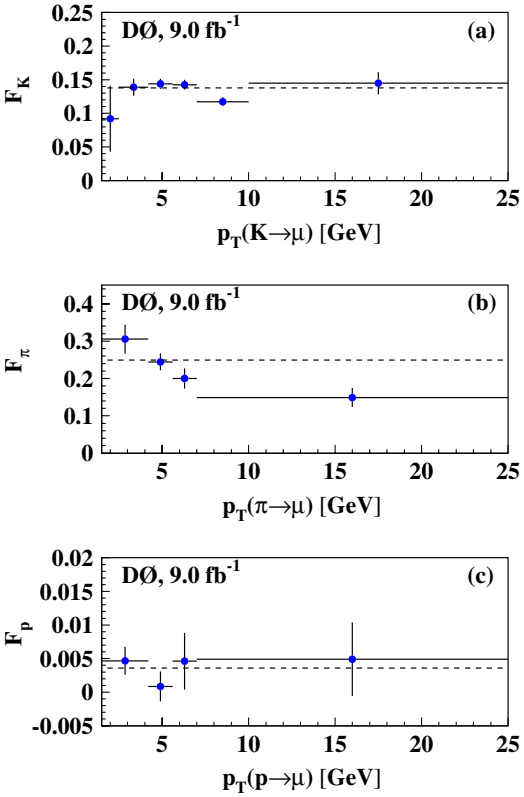

FIG. 12 (color online). The values of (a) F_K, (b) F_π and (c) F_p in the like-sign dimuon sample as a function of the kaon, pion and proton p_T, respectively. The horizontal dashed lines show the mean values.

TABLE VI. Values of F_K, F_π, and F_p for different p_T bins. The last line shows the weighted average of these quantities obtained with weights given by the fraction of muons in a given p_T interval F_μ^i in the dimuon sample, see Table I. Only statistical uncertainties are given.

Bin	$F_K \times 10^2$	$F_\pi \times 10^2$	$F_p \times 10^2$
1	9.19 ± 4.90	30.54 ± 3.89	0.47 ± 0.21
2	13.88 ± 1.26		
3	14.38 ± 0.74	24.43 ± 2.28	0.09 ± 0.22
4	14.26 ± 0.74	19.99 ± 2.67	0.46 ± 0.42
5	11.73 ± 0.67	14.90 ± 2.55	0.49 ± 0.55
6	14.48 ± 1.64		
All	13.78 ± 0.38	24.81 ± 1.34	0.35 ± 0.14

measurement [11], this uncertainty was 3.6%, and was based on simulation of the events.

Using the extracted values of R_K, we derive the values of F_K, F_π and F_p. The computation of F_K is done using Eq. (16), and we follow the procedure described in Ref. [11] to determine F_π and F_p. The results are shown in Fig. 12 and in Table VI. The fractions F_π and F_p are poorly determined for the lowest and highest p_T because of the small number of events. The content of bins 1 and 2, and bins 5 and 6, are therefore combined.

VI. SYSTEMATIC UNCERTAINTIES FOR BACKGROUND FRACTIONS

The systematic uncertainties for the background fractions are discussed in Ref. [11], and we only summarize the values used in this analysis. The systematic uncertainty on the fraction f_K is set to 9% [11]. The systematic uncertainty on the ratio R_K, as indicated in Sec. V, is set to half of the uncertainty on ΔR_K given in Eq. (24). The systematic uncertainties on the ratios of multiplicities n_π/n_K and n_p/n_K in $p\bar{p}$ interactions are set to 4% [17]. These multiplicities are required to compute the quantities f_π, f_p. The ratios N_π/N_K and N_p/N_K, required to compute the quantities F_π and F_p [11] are assigned an additional 4% systematic uncertainty. The values of these uncertainties are discussed in Ref. [11].

VII. MEASUREMENT OF f_S, F_{SS}

We determine the fraction f_S of S muons in the inclusive-muon sample and the fraction F_{SS} of events with two S muons in the like-sign dimuon sample following the procedure described in Ref. [11]. We use the following value from simulation

$$\frac{F_{LL}}{F_{SL} + F_{LL}} = 0.264 \pm 0.024, \tag{25}$$

and obtain

$$\begin{aligned} f_S &= 0.536 \pm 0.017(\text{stat}) \pm 0.043(\text{syst}), \\ F_{\text{bkg}} &= 0.389 \pm 0.019(\text{stat}) \pm 0.038(\text{syst}), \\ F_{LL} &= 0.082 \pm 0.005(\text{stat}) \pm 0.010(\text{syst}), \\ F_{SL} &= F_{\text{bkg}} - 2F_{LL}, \\ F_{SS} &= 0.692 \pm 0.015(\text{stat}) \pm 0.030(\text{syst}). \end{aligned} \tag{26}$$

The differences between these values and that in Ref. [11] are due to the increased statistics and the changes in the muon selection and in the analysis procedure.

VIII. MEASUREMENT OF a_K, a_π, a_p, δ

We measure all detector-related asymmetries using the methods presented in Ref. [11]. Muons from decays of charged kaons and pions and from incomplete absorption of hadrons that penetrate the calorimeter and reach the muon detectors (''punch through''), as well as false matches of central tracks to segments reconstructed in the outer muon detector, are considered as detector backgrounds. We use data to measure the fraction of each source of background in both the dimuon and inclusive-muon samples, and the corresponding asymmetries. Data are also used to determine the intrinsic charge-detection asymmetry of the D0 detector. Since the interaction length of the K^+ meson is greater than that of the K^- meson [14], kaons provide a positive contribution to the asymmetries A

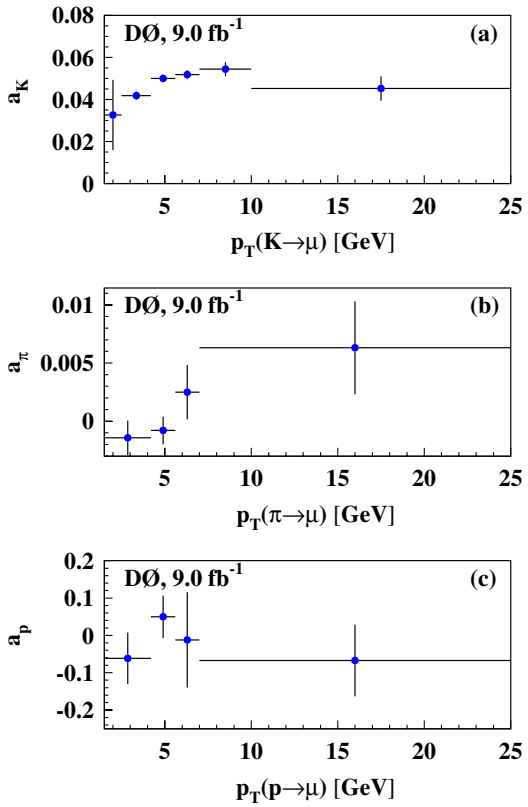

FIG. 13 (color online). The asymmetries (a) a_K, (b) a_π, and (c) a_p as a function of the kaon, pion and proton p_T, respectively.

TABLE VII. Asymmetries a_K, a_π, and a_p for different p_T bins. The bottom row shows the mean asymmetries averaged over the inclusive-muon sample. Only the statistical uncertainties are given.

Bin	$a_K \times 10^2$	$a_\pi \times 10^2$	$a_p \times 10^2$
1	$+3.26 \pm 1.67$	-0.14 ± 0.15	-6.2 ± 6.9
2	$+4.18 \pm 0.20$		
3	$+5.00 \pm 0.13$	-0.08 ± 0.12	$+4.9 \pm 5.6$
4	$+5.18 \pm 0.22$	$+0.25 \pm 0.23$	-1.2 ± 12.8
5	$+5.44 \pm 0.34$	$+0.63 \pm 0.40$	-6.8 ± 9.6
6	$+4.52 \pm 0.57$		
All	$+4.88 \pm 0.09$	-0.03 ± 0.08	-0.8 ± 3.8

TABLE VIII. Muon reconstruction asymmetry δ_i for different muon p_T bins. Only the statistical uncertainties are given.

Bin	$\delta_i \times 10^2$
1	-0.509 ± 0.106
2	-0.205 ± 0.040
3	-0.053 ± 0.048
4	-0.124 ± 0.075
5	$+0.050 \pm 0.099$
6	$+0.034 \pm 0.189$

and a. The asymmetries for other background sources (pions, protons, and falsely reconstructed tracks) are at least a factor of 10 smaller.

The results for the asymmetries a_K, a_π, and a_p in different muon p_T bins are shown in Fig. 13 and Table VII. The asymmetries a_π and a_p are poorly measured in the first and last bins due to the small number of events. The content of bins 1 and 2, and bins 5 and 6, are therefore combined.

The small residual reconstruction asymmetry δ_i is measured using a sample of $J/\psi \to \mu^+\mu^-$ decays reconstructed from two central detector tracks, with at least one matching a track segment in the muon detector. The values of δ_i obtained as a function of muon p_T, are given in Table VIII and are shown in Fig. 14. The weighted averages for the residual muon asymmetry in the inclusive-muon and the like-sign dimuon samples, calculated using weights given by the fraction of muons in each p_T interval f^i_μ (F^i_μ) in the inclusive-muon (dimuon) sample, are given by

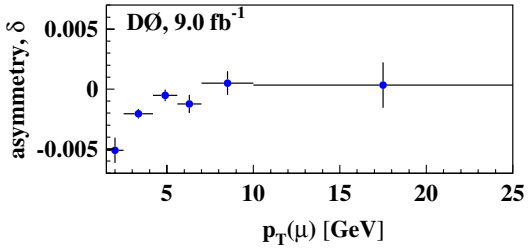

FIG. 14 (color online). Muon reconstruction asymmetry as a function of muon p_T.

$$\delta \equiv \sum_{i=1}^{6} f^i_\mu \delta_i = (-0.088 \pm 0.023)\%, \quad (27)$$

$$\Delta \equiv \sum_{i=1}^{6} F^i_\mu \delta_i = (-0.132 \pm 0.019)\%, \quad (28)$$

where only the statistical uncertainties are given. The correlations among different δ_i are taken into account in the uncertainties in Eqs. (27) and (28).

IX. CORRECTIONS FOR BACKGROUND ASYMMETRIES

The corrections for the background and detector contributions to the measured raw asymmetries a and A are obtained combining the results from Tables I, III, VI, and VII, and summarized in Tables IX and X. The values in the bottom row of these tables are computed by averaging the corresponding quantities with weights given by the fraction of muons in each p_T interval f^i_μ (F^i_μ) in the inclusive-muon (dimuon) sample, see Eqs. (7) and (8). We use the mean values for f_π, F_π, f_p, F_p, a_π, and a_p in bins 1 and 2, and in bins 5 and 6, as the number of events for those bins are not sufficient to perform separate measurements.

TABLE IX. Corrections due to background asymmetries $f_K a_K$, $f_\pi a_\pi$, and $f_p a_p$ for different p_T bins. The bottom row shows the weighted averages obtained using weights given by the fraction of muons in a given p_T interval, f^i_μ, in the inclusive-muon sample. Only statistical uncertainties are given.

Bin	$f_K a_K \times 10^2$	$f_\pi a_\pi \times 10^2$	$f_p a_p \times 10^2$
1	$+0.305 \pm 0.220$	-0.052 ± 0.054	-0.034 ± 0.041
2	$+0.624 \pm 0.052$		
3	$+0.832 \pm 0.030$	-0.025 ± 0.037	$+0.005 \pm 0.016$
4	$+0.912 \pm 0.046$	$+0.068 \pm 0.065$	-0.008 ± 0.081
5	$+0.785 \pm 0.054$	$+0.121 \pm 0.079$	-0.043 ± 0.077
6	$+0.577 \pm 0.086$		
All	$+0.776 \pm 0.021$	$+0.007 \pm 0.027$	-0.014 ± 0.022

TABLE X. Corrections due to background asymmetries $F_K a_K$, $F_\pi a_\pi$ and $F_p a_p$ for different p_T bins. The bottom row shows the weighted averages obtained using weights given by the fraction of muons in a given p_T interval, F^i_μ, in the like-sign dimuon sample. Only statistical uncertainties are given.

Bin	$F_K a_K \times 10^2$	$F_\pi a_\pi \times 10^2$	$F_p a_p \times 10^2$
1	$+0.300 \pm 0.222$	-0.044 ± 0.046	-0.029 ± 0.035
2	$+0.581 \pm 0.060$		
3	$+0.719 \pm 0.042$	-0.020 ± 0.029	$+0.004 \pm 0.012$
4	$+0.739 \pm 0.050$	$+0.050 \pm 0.047$	-0.005 ± 0.059
5	$+0.638 \pm 0.054$	$+0.094 \pm 0.062$	-0.033 ± 0.060
6	$+0.655 \pm 0.112$		
All	$+0.633 \pm 0.031$	-0.002 ± 0.023	-0.016 ± 0.019

TABLE XI. Heavy-quark decays contributing to the inclusive-muon and like-sign dimuon samples [17]. The abbreviation "nonosc" stands for "nonoscillating," and "osc" for "oscillating." All weights are computed using MC simulation.

	Process	Weight
T_1	$b \to \mu^- X$	$w_1 \equiv 1.$
T_{1a}	$b \to \mu^- X$ (nonosc)	$w_{1a} = (1 - \chi_0)w_1$
T_{1b}	$\bar{b} \to b \to \mu^- X$ (osc)	$w_{1b} = \chi_0 w_1$
T_2	$b \to c \to \mu^+ X$	$w_2 = 0.096 \pm 0.012$
T_{2a}	$b \to c \to \mu^+ X$ (nonosc)	$w_{2a} = (1 - \chi_0)w_2$
T_{2b}	$\bar{b} \to b \to c \to \mu^+ X$ (osc)	$w_{2b} = \chi_0 w_2$
T_3	$b \to c\bar{c}q$ with $c \to \mu^+ X$ or $\bar{c} \to \mu^- X$	$w_3 = 0.064 \pm 0.006$
T_4	η, ω, ρ^0, $\phi(1020)$, J/ψ, $\psi' \to \mu^+\mu^-$	$w_4 = 0.021 \pm 0.002$
T_5	$b\bar{b}c\bar{c}$ with $c \to \mu^+ X$ or $\bar{c} \to \mu^- X$	$w_5 = 0.013 \pm 0.002$
T_6	$c\bar{c}$ with $c \to \mu^+ X$ or $\bar{c} \to \mu^- X$	$w_6 = 0.675 \pm 0.101$

X. COEFFICIENTS c_b AND C_b

The dilution coefficients c_b and C_b in Eq. (12) are obtained through simulations using the method described in Ref. [11]. Both coefficients depend on the value of the mean mixing probability, χ_0. We use the value obtained at LEP as averaged by HFAG [3] for this measurement

$$\chi_0(\text{HFAG}) = 0.1259 \pm 0.0042. \tag{29}$$

To measure the weights for the different processes producing S muons, we correct the momentum distribution of generated b hadrons to match that in the data used in this analysis. The determined weights [17] are given in Table XI.

The uncertainty on the weights for the different processes contains contributions from the uncertainty in the momentum of the generated b hadrons and from the uncertainties in b-hadron branching fractions. The difference in the weights with and without the momentum correction contributes to the assigned uncertainties. Additional contributions to the uncertainties on the weights derive from the uncertainties on the inclusive branching fractions $B \to \mu X$, $B \to cX$ and $B \to \bar{c}X$ [14]. We assign an additional uncertainty of 15% to the weights w_5 and w_6 for uncertainties on the cross sections for $c\bar{c}$ and $b\bar{b}c\bar{c}$ production.

The resulting c_b and C_b coefficients are found to be

$$c_b = +0.061 \pm 0.007, \tag{30}$$

$$C_b = +0.474 \pm 0.032. \tag{31}$$

XI. ASYMMETRY A^b_{sl}

The results obtained in Secs. IV, V, VI, VII, VIII, IX, and X are used to measure the asymmetry A^b_{sl} following the procedure of Ref. [11]. Using 2.041×10^9 muons in the inclusive-muon sample and 6.019×10^6 events in the like-sign dimuon sample we obtain the following values for the uncorrected asymmetries a and A:

$$a = (+0.688 \pm 0.002)\%, \tag{32}$$

$$A = (+0.126 \pm 0.041)\%. \tag{33}$$

The difference between these values and those in Ref. [11] are due to increased statistics and the changes in the muon selection. The contributions from different background sources to the observed asymmetries a and A are summarized in Table XII.

The asymmetry A^b_{sl}, extracted from the asymmetry a of the inclusive-muon sample using Eqs. (7) and (30), is

$$A^b_{\text{sl}} = (-1.04 \pm 1.30(\text{stat}) \pm 2.31(\text{syst}))\%. \tag{34}$$

The contributions to the uncertainty are given in Table XIII. Figure 15(a) shows a comparison of the asymmetry a and the background asymmetry, $a_{\text{bkg}} = f_S\delta + f_K a_K + f_\pi a_\pi + f_p a_p$, as a function of muon p_T. There is excellent agreement between these two quantities, with $\chi^2/\text{d.o.f.} = 0.8/6$ for their difference. Figure 15(b) shows the value of $f_S a_S = a - a_{\text{bkg}}$, which is consistent with zero. The values a and a_{bkg} are given in Table XIV. This result agrees with the expectation that the value of the asymmetry a is determined mainly by the background, as the contribution from A^b_{sl} is strongly suppressed by the factor of $c_b = 0.061 \pm 0.007$. The consistency of A^b_{sl} with zero in Eq. (34) and the good description of the charge asymmetry a for different values of muon p_T shown in Fig. 15 constitute important tests of the validity of the background model and of the method of analysis discussed in this article.

The second measurement of the asymmetry A^b_{sl}, obtained from the uncorrected asymmetry A of the like-sign dimuon sample using Eqs. (8), (30), and (31), is

$$A^b_{\text{sl}} = (-0.808 \pm 0.202(\text{stat}) \pm 0.222(\text{syst}))\%, \tag{35}$$

TABLE XII. Contribution of different background sources to the observed asymmetry in the inclusive-muon and like-sign dimuon samples. Only statistical uncertainties are given.

Source	inclusive-muon	like-sign dimuon
$(f_K a_K$ or $F_K a_K) \times 10^2$	$+0.776 \pm 0.021$	$+0.633 \pm 0.031$
$(f_\pi a_\pi$ or $F_\pi a_\pi) \times 10^2$	$+0.007 \pm 0.027$	-0.002 ± 0.023
$(f_p a_p$ or $F_p a_p) \times 10^2$	-0.014 ± 0.022	-0.016 ± 0.019
$[(1 - f_{\text{bkg}})\delta$ or $(2 - F_{\text{bkg}})\Delta] \times 10^2$	-0.047 ± 0.012	-0.212 ± 0.030
$(a_{\text{bkg}}$ or $A_{\text{bkg}}) \times 10^2$	$+0.722 \pm 0.042$	$+0.402 \pm 0.053$
$(a$ or $A) \times 10^2$	$+0.688 \pm 0.002$	$+0.126 \pm 0.041$
$[(a - a_{\text{bkg}})$ or $(A - A_{\text{bkg}})] \times 10^2$	-0.034 ± 0.042	-0.276 ± 0.067

TABLE XIII. Sources of uncertainty on $A^b_{\rm sl}$ from Eqs. (34)–(36). The first nine rows contain statistical uncertainties, while the next four rows reflect contributions from systematic uncertainties.

Source	$\delta(A^b_{\rm sl}) \times 10^2$ Eq. (34)	$\delta(A^b_{\rm sl}) \times 10^2$ Eq. (35)	$\delta(A^b_{\rm sl}) \times 10^2$ Eq. (36)
A or a (stat)	0.068	0.121	0.132
f_K (stat)	0.472	0.064	0.028
R_K (stat)	N/A	0.059	0.065
$P(\pi \to \mu)/P(K \to \mu)$	0.181	0.023	0.008
$P(p \to \mu)/P(K \to \mu)$	0.323	0.026	0.002
A_K	0.458	0.052	0.037
A_π	0.802	0.067	0.030
A_p	0.584	0.050	0.020
δ or Δ	0.377	0.087	0.067
f_K (syst)	2.310	0.204	0.007
R_K (syst)	N/A	0.068	0.072
π, K, p multiplicity	0.067	0.019	0.017
c_b or C_b	0.121	0.052	0.056
Total statistical	1.304	0.202	0.172
Total systematic	2.313	0.222	0.093
Total	2.656	0.300	0.196

where we take into account that both a_S and A_S in Eq. (8) are proportional to $A^b_{\rm sl}$, and that $F_{SS}C_b + F_{SL}c_b = 0.342 \pm 0.028$. The contributions to the uncertainty of $A^b_{\rm sl}$ for this measurement are also listed in Table XIII.

The measurement of the asymmetry $A^b_{\rm sl}$ using the linear combination given in Eq. (13) is performed following the procedure described in Ref. [11]. We select the value of the parameter α that minimizes the total uncertainty on the $A^b_{\rm sl}$ measurement. Appendix A gives more details on this method of combination. All uncertainties in Table XIII, except the statistical uncertainties on a, A, and R_K, are treated as fully correlated. This leads to $\alpha = 0.89$, and the corresponding value of the asymmetry $A^b_{\rm sl}$ is

$$A^b_{\rm sl} = (-0.787 \pm 0.172(\text{stat}) \pm 0.093(\text{syst}))\%. \quad (36)$$

This value is used as the final result for $A^b_{\rm sl}$. It differs by 3.9 standard deviations from the standard model prediction of $A^b_{\rm sl}$ given in Eq. (5). The different contributions to the total uncertainty on $A^b_{\rm sl}$ in Eq. (36) are listed in Table XIII.

The measured value of $A^b_{\rm sl}$ places a constraint on the charge asymmetries $a^d_{\rm sl}$ and $a^s_{\rm sl}$. The asymmetry $A^b_{\rm sl}$ is a linear combination of the semileptonic charge asymmetries from B^0 and B^0_s meson decays [2]. The coefficients C_d and C_s in Eq. (2) depend on the mean mixing probabilities and the production fractions of B^0 and B^0_s mesons. We use the production fractions measured at LEP as averaged by HFAG [3]

$$f_d(\text{HFAG}) = 0.403 \pm 0.009, \quad (37)$$

$$f_s(\text{HFAG}) = 0.103 \pm 0.009, \quad (38)$$

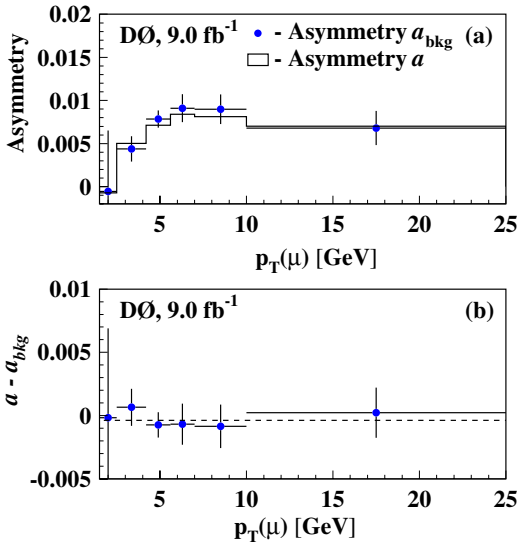

FIG. 15 (color online). (a) The asymmetry $a_{\rm bkg}$ (points with error bars representing the total uncertainties), expected from the measurements of the fractions and asymmetries for background processes, is compared to the measured asymmetry a for the inclusive-muon sample (shown as a histogram, since the statistical uncertainties are negligible). The asymmetry from CP violation is negligible compared to the background in the inclusive-muon sample. (b) The difference $a - a_{\rm bkg}$. The horizontal dashed line shows the mean value.

and find the values given in Eq. (4). The difference in the fragmentation functions of B^0 and B^0_s mesons can change the values of C_d and C_s [18]. However, the experimental information on this difference is insufficient and we do not consider it in our measurement.

Figure 16 presents the measurement in the $(a^d_{\rm sl}, a^s_{\rm sl})$ plane together with the existing direct measurements of $a^d_{\rm sl}$ from the B factories [3] and the independent D0 measurement of $a^s_{\rm sl}$ in $B^0_s \to \mu D_s X$ decays [19]. All measurements are consistent.

The quantity $A_{\rm res}$ defined as

$$A_{\rm res} \equiv (A - \alpha a) - (A_{\rm bkg} - \alpha a_{\rm bkg}) \quad (39)$$

is the residual charge asymmetry of like-sign dimuon events after subtracting all background contributions

TABLE XIV. The measured asymmetry a and the expected background asymmetry $a_{\rm bkg}$ in the inclusive-muon sample for different p_T bins. For the background asymmetry, the first uncertainty is statistical, the second is systematic.

bin	$a \times 10^2$	$a_{\rm bkg} \times 10^2$
1	-0.071 ± 0.025	$-0.055 \pm 0.240 \pm 0.664$
2	$+0.503 \pm 0.005$	$+0.438 \pm 0.089 \pm 0.117$
3	$+0.712 \pm 0.003$	$+0.785 \pm 0.056 \pm 0.083$
4	$+0.841 \pm 0.005$	$+0.910 \pm 0.124 \pm 0.105$
5	$+0.812 \pm 0.007$	$+0.897 \pm 0.139 \pm 0.101$
6	$+0.702 \pm 0.010$	$+0.680 \pm 0.189 \pm 0.059$

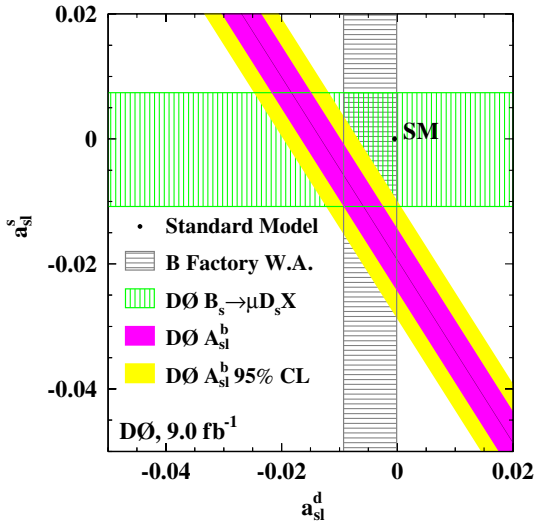

FIG. 16 (color online). Comparison of $A_{\rm sl}^b$ in data with the SM prediction for $a_{\rm sl}^d$ and $a_{\rm sl}^s$. Also shown are the measurements of $a_{\rm sl}^d$ [3] and $a_{\rm sl}^s$ [19]. The error bands represent the ± 1 standard deviation uncertainties on each individual measurement. The 95% CL band is also given for this $A_{\rm sl}^b$ measurement.

from the raw charge asymmetry. This quantity does not depend on the interpretation in terms of the charge asymmetry of semileptonic decays of B mesons. We obtain

$$A_{\rm res} = (-0.246 \pm 0.052({\rm stat}) \pm 0.021({\rm syst}))\%, \quad (40)$$

The measured value of $A_{\rm res}$ differs by 4.2 standard deviations from the standard model prediction

$$A_{\rm res}({\rm SM}) = (-0.009 \pm 0.002)\%. \quad (41)$$

XII. CONSISTENCY CHECKS

To study the stability of the result, we repeat this measurement with modified selections, and with subsets of the available data. The only difference compared to Ref. [11] is Test D, where we applied a stronger criterion on the muon IP, following the suggestion of Ref. [20]. In all tests the modified selections were applied to all muons. For completeness, we give the full list of tests performed:

(i) Test A1: Using only the part of the data sample corresponding to the first 2.8 fb^{-1}.
(ii) Test A2: Using only the part of the data sample corresponding to the previous measurement with 6.1 fb^{-1} [11].
(iii) Test A3: Using only the part of the data sample corresponding to the last 2.9 fb^{-1}.
(iv) Test B: In addition to the reference muon selections [11], we require at least three hits in the muon wire chambers (layers B or C), and lower the χ^2 requirement for the fit to a track segment reconstructed in the muon detector.
(v) Test C: Since background muons are mainly produced by decays of kaons and pions, their track parameters measured in the central tracker and by the muon system can differ. The background fraction therefore depends strongly on the χ^2 of the difference between these two measurements. The requirement on this χ^2 is changed from 12 to 4.
(vi) Test D: The maximum value of the IP is changed from 0.3 to 0.012 cm. This test is also sensitive to possible contamination from cosmic-ray muons.
(vii) Test E: Using low-luminosity data with fewer than three interaction vertices.
(viii) Test F: Using events corresponding to only two of four possible configurations for the magnets, with identical solenoid and toroid polarities.
(ix) Test G: Changing the minimum requirement on the invariant mass of the two muons from 2.8 GeV to 12 GeV.
(x) Test H: Using the same muon p_T requirement, $p_T > 4.2$ GeV, for the full detector acceptance.
(xi) Test I: Requiring the muon p_T to be $p_T < 7.0$ GeV.
(xii) Test J: Requiring the azimuthal angle ϕ of the muon track to be in the range $0 < \phi < 4$ or $5.7 < \phi < 2\pi$. This selection excludes muons with reduced muon identification efficiency in the region of the support structure of the detector.
(xiii) Test K: Requiring the muon η to be in the range $|\eta| < 1.6$. This test is sensitive to possible contamination from muons associated with beam halos.
(xiv) Test L: Requiring the muon η to have $|\eta| < 1.2$ or $1.6 < |\eta| < 2.2$.
(xv) Test M: Requiring the muon η to be in the range $|\eta| < 0.7$ or $1.2 < |\eta| < 2.2$.
(xvi) Test N: Requiring the muon η to be in the range $0.7 < |\eta| < 2.2$.
(xvii) Test O: Using like-sign dimuon events that pass at least one single muon trigger, while ignoring the requirement for a dimuon trigger.
(xviii) Test P: Using like-sign dimuon events passing both single muon and dimuon triggers.

A summary of these studies is presented in Tables XV and XVI. The last row, denoted as "Significance", gives the absolute value of the difference between the reference result (column Ref) and each modification, divided by its uncertainty, taking into account the overlap in events between the reference and test samples. Both statistical and systematic uncertainties are used in the calculation of the significance of the difference. The χ^2 of these tests defined as the sum of the square of all significances is $\chi^2 = 17.1$ for 18 tests. These tests demonstrate the stability of the measured asymmetry $A_{\rm sl}^b$, and provide a confirmation of the validity of the method.

We also compare the dependence on the muon pseudorapidity $\eta(\mu)$ of the observed and expected charge asymmetry in the inclusive-muon sample. We repeat the analysis procedure, but measure all background contributions as a

TABLE XV. Measured asymmetry $A^b_{\rm sl}$ for the reference selection (column Ref) and for samples used in Tests A–H.

	Ref	A1	A2	A3	B	C	D	E	F	G	H
$N(\mu\mu)\times 10^{-6}$	6.019	1.932	3.991	2.028	4.466	3.280	2.857	3.128	3.012	2.583	2.220
$a\times 10^2$	+0.688	+0.703	+0.680	+0.702	+0.548	+0.325	+0.835	+0.682	+0.727	+0.688	+0.751
$A\times 10^2$	+0.126	+0.061	+0.062	+0.259	−0.149	−0.361	+0.555	+0.136	+0.137	+0.450	+0.344
α	0.894	0.760	0.851	0.813	0.891	0.631	1.271	0.831	0.940	0.939	0.807
$[(2-F_{\rm bkg})\Delta-\alpha f_S\delta]\times 10^2$	−0.170	−0.193	−0.178	−0.157	−0.270	−0.370	−0.133	−0.206	−0.152	−0.114	−0.049
f_S	0.536	0.583	0.557	0.516	0.509	0.560	0.472	0.534	0.493	0.537	0.536
$F_{\rm bkg}$	0.389	0.336	0.365	0.384	0.405	0.338	0.627	0.374	0.407	0.436	0.325
$A^b_{\rm sl}\times 10^2$	−0.787	−0.803	−0.891	−0.600	−0.906	−0.708	−1.138	−0.584	−0.986	−0.379	−0.654
$\sigma(A^b_{\rm sl})\times 10^2$ (stat)	0.172	0.278	0.204	0.335	0.207	0.220	0.365	0.224	0.302	0.263	0.254
$\sigma(A^b_{\rm sl})\times 10^2$ (syst)	0.093	0.125	0.128	0.188	0.107	0.104	0.323	0.108	0.135	0.209	0.103
Significance		0.007	0.742	0.567	1.029	0.525	1.022	1.236	0.960	1.537	1.120

TABLE XVI. Measured asymmetry $A^b_{\rm sl}$ for the reference selection (column Ref) and for samples used in Tests I–P.

	Ref	I	J	K	L	M	N	O	P
$N(\mu\mu)\times 10^{-6}$	6.019	4.428	3.504	2.928	2.741	4.259	3.709	2.724	2.440
$a\times 10^2$	+0.688	+0.672	+0.691	+0.711	+0.761	+0.501	+0.802	+0.688	+0.688
$A\times 10^2$	+0.126	+0.250	+0.160	+0.118	+0.216	−0.033	+0.262	+0.245	+0.272
α	0.894	0.908	0.817	0.872	0.825	0.702	0.908	0.941	0.898
$[(2-F_{\rm bkg})\Delta-\alpha f_S\delta]\times 10^2$	−0.170	−0.209	−0.187	−0.221	−0.214	−0.187	−0.150	−0.126	−0.122
f_S	0.536	0.514	0.555	0.556	0.570	0.519	0.514	0.536	0.536
$F_{\rm bkg}$	0.389	0.414	0.352	0.363	0.333	0.402	0.428	0.408	0.395
$A^b_{\rm sl}\times 10^2$	−0.787	−0.925	−0.569	−0.847	−0.430	−0.761	−0.774	−0.809	−0.689
$\sigma(A^b_{\rm sl})\times 10^2$ (stat)	0.172	0.204	0.202	0.224	0.260	0.207	0.221	0.247	0.253
$\sigma(A^b_{\rm sl})\times 10^2$ (syst)	0.093	0.115	0.100	0.122	0.117	0.110	0.118	0.129	0.128
Significance		1.245	1.672	0.377	1.678	0.441	0.186	0.120	0.497

function of $|\eta(\mu)|$. The result of this comparison is shown in Fig. 17. The dependence on $|\eta(\mu)|$ is correctly described by the background asymmetry. There is good agreement between these two quantities, with a $\chi^2/\text{d.o.f.} = 2.8/4$. This is consistent with our expectation that the contribution of $A^b_{\rm sl}$ in the inclusive-muon charge asymmetry is overwhelmed by background.

Figure 18 shows the observed and expected uncorrected like-sign dimuon charge asymmetry as a function of the dimuon invariant mass. The expected asymmetry is computed using Eq. (8) and the measured parameters of sample composition and asymmetries. As in Ref. [11], we compare the expected uncorrected asymmetry using two assumptions for $A^b_{\rm sl}$. In Fig. 18(a) the observed asymmetry is compared to the expectation for the SM value of $A^b_{\rm sl}(\text{SM}) = -0.028\%$, while Fig. 18(b) shows the expected asymmetry for $A^b_{\rm sl} = -0.787\%$. Large discrepancies between the observed and expected asymmetries can be observed for $A^b_{\rm sl} = A^b_{\rm sl}(\text{SM})$, while good agreement is obtained for the measured $A^b_{\rm sl}$ value corresponding to Eq. (36). The observed asymmetry changes as a function of dimuon invariant mass, and the expected asymmetry tracks this effect when $A^b_{\rm sl} = -0.787\%$. This dependence of the asymmetry on invariant mass of the muon pair is a function

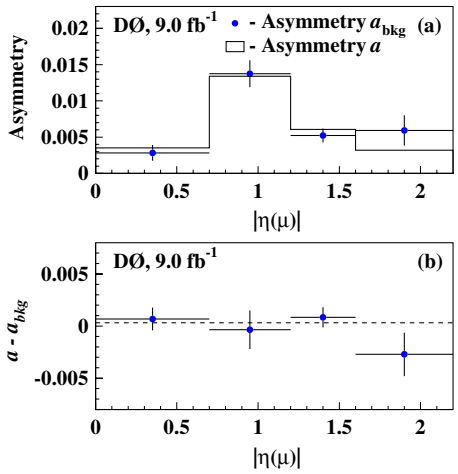

FIG. 17 (color online). (a) The asymmetry $a_{\rm bkg}$ (points with error bars representing the total uncertainties), as expected from the measurements of the fractions and asymmetries of the background processes, is compared to the measured asymmetry a of the inclusive-muon sample (shown as a histogram, since the statistical uncertainties are negligible) as a function of the absolute value of muon pseudorapidity $|\eta(\mu)|$. The asymmetry from CP violation is negligible compared to the background in the inclusive-muon sample. (b) The difference $a - a_{\rm bkg}$. The horizontal dashed line shows the mean value.

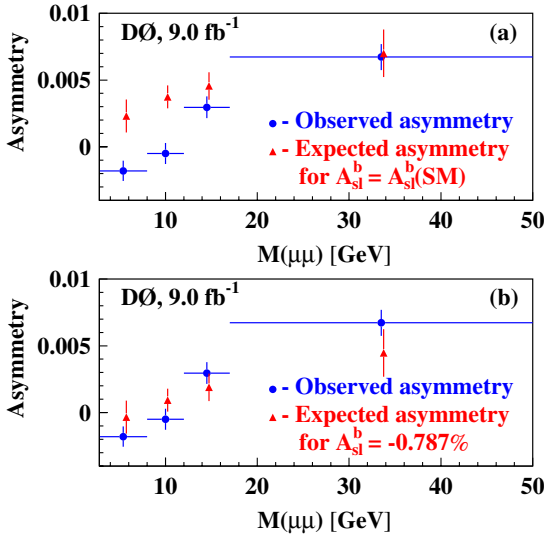

FIG. 18 (color online). The observed and expected like-sign dimuon charge asymmetries in bins of dimuon invariant mass. The expected asymmetry is shown for (a) $A^b_{\rm sl} = A^b_{\rm sl}({\rm SM})$ and (b) $A^b_{\rm sl} = -0.787\%$.

of the production mechanism of the particles involved and of their decays. The agreement between the observed and expected asymmetries indicates that the physics leading to the observed asymmetry can be described by contributions from the background and from decays of b hadrons.

We also measure the mean mixing probability using the ratio of like-sign and opposite-sign dimuon events. The background contribution in both samples is obtained using the method presented in this article. The measured mean mixing probability is found to be consistent with the world average value [3].

We conclude that our method of analysis provides a consistent description of the dimuon charge asymmetry for a wide range of input parameters, as well as for significantly modified selection criteria.

XIII. COMPARISON WITH SIMULATION

The measurement of the background fractions is based on data, and the input from simulation is limited to the ratio of multiplicities n_π/n_K and n_p/n_K in $p\bar{p}$ interactions [11]. Nevertheless, it is instructive to compare the results obtained in data and in simulation. Such a comparison is shown in Table XVII. The simulation used in this analysis is described in Ref. [11]. All quantities measured in simulation are obtained using the information on the generated processes. All uncertainties in the second and third columns are statistical. The difference between the values obtained in data and simulation is given in the fourth column and includes the systematic uncertainties. The agreement between the measured and simulated quantities is satisfactory. The excellent agreement between the mean values of R_K, which is one of the most essential quantities of this measurement and for which many systematic uncertainties cancel, is especially notable

$$R_K({\rm data}) = 0.856 \pm 0.020({\rm stat}) \pm 0.026({\rm syst}),$$
$$R_K({\rm MC}) = 0.901 \pm 0.086({\rm MC\ stat}). \quad (42)$$

This comparison provides support for the validity of the presented measurement.

TABLE XVII. Comparison of background fractions measured in data and in simulation. Only the statistical uncertainties are given in the second and third column. The difference between data and simulation is given in the fourth column and includes both statistical and systematic uncertainties.

Quantity	Data	Simulation	Difference
$f_K \times 10^2$	15.96 ± 0.24	14.31 ± 0.06	$+1.65 \pm 2.55$
$f_\pi \times 10^2$	30.01 ± 1.60	29.82 ± 0.09	$+0.19 \pm 5.15$
$f_p \times 10^2$	0.38 ± 0.17	1.07 ± 0.02	-0.69 ± 0.60
$F_K \times 10^2$	13.78 ± 0.42	12.89 ± 1.32	$+0.89 \pm 2.26$
$F_\pi \times 10^2$	24.81 ± 1.38	25.88 ± 1.86	-1.07 ± 4.36
$F_p \times 10^2$	0.35 ± 0.14	1.29 ± 0.39	-0.94 ± 0.72
$f_S \times 10^2$	53.65 ± 1.74	54.79 ± 0.14	-1.14 ± 7.11
$F_{\rm bkg} \times 10^2$	38.94 ± 1.89	40.01 ± 2.31	-1.07 ± 6.21
$R_K \times 10^2$	85.62 ± 1.98	90.08 ± 8.60	-4.46 ± 9.74

XIV. DEPENDENCE OF ASYMMETRY $A^b_{\rm sl}$ ON MUON IMPACT PARAMETER

The asymmetry $A^b_{\rm sl}$ is produced by muons from direct semileptonic decays of b quarks. A distinctive feature of these muons is the large impact parameter of their trajectories with respect to the primary vertex [12,20]. The simulation shows that the dominant source of background from L muons corresponds to charged hadrons produced in the primary interactions that then decay to muons, and the tracks of such muons have small impact parameters if the decay is outside the tracking volume. Figure 19 shows the muon IP distribution in data and in simulation. The shaded histogram shows the contribution from L muons in simulation, which decreases significantly for increasing values of the muon IP. The background can therefore be significantly suppressed by selecting muons with large impact parameter.

To verify the origin of the observed charge asymmetry, we perform several complementary measurements. We require the muon IP to be larger or smaller than 120 μm. For events in the like-sign dimuon sample, we require that both muons satisfy these conditions. These measurements are denoted as $\mathrm{IP}_{>120}$ and $\mathrm{IP}_{<120}$, respectively. The selected threshold of 120 μm can be compared with the spread in the crossing point of the colliding beams in the Tevatron collider, and with the precision of $p\bar{p}$ vertex

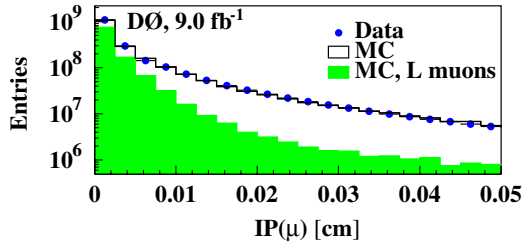

FIG. 19 (color online). The muon IP distribution in the inclusive-muon sample (bullets). The solid line represents the muon IP distribution in simulation. The shaded histogram is the contribution from L muons in simulation.

reconstruction, which are about 30 μm and 15 μm, respectively, in the plane perpendicular to the beam axis. The chosen value of 120 μm gives the minimal uncertainty on $a^d_{\rm sl}$ and $a^s_{\rm sl}$ defined in Eq. (2). The measurement of these asymmetries using the combination of $A^b_{\rm sl}$ measurements with IP above and below the chosen cut is discussed below in this section.

In total, 0.356×10^9 muons in the inclusive-muon sample and 0.714×10^6 events in the like-sign dimuon sample are selected for the $\mathrm{IP}_{>120}$ measurement. Events are subject to the same analysis as for the entire sample, except that the ratio $R_K(K^0_S)$ is not used because of insufficient $K^0_S \to \pi^+\pi^-$ decays in the dimuon sample. Background asymmetries should not depend on the muon IP, and we verified that the difference in kaon asymmetry for the whole sample and the $\mathrm{IP}_{>120}$ events agree: $a_K(\mathrm{IP}_{>120}) - a_K(\mathrm{all}) = (-1.6 \pm 1.5)\%$. We therefore use the values given in Tables VII and VIII. All other measured quantities are given in Table XVIII. The background fractions are strongly suppressed in the $\mathrm{IP}_{>120}$ sample, and their influence on the measurement of $A^b_{\rm sl}$ is significantly smaller. Using these values, we obtain for the inclusive-muon sample

$$A^b_{\rm sl}(\mathrm{IP}_{>120}) = (-0.422 \pm 0.240(\mathrm{stat}) \pm 0.121(\mathrm{syst}))\%, \quad (43)$$

and for the like-sign dimuon sample

$$A^b_{\rm sl}(\mathrm{IP}_{>120}) = (-0.818 \pm 0.342(\mathrm{stat}) \pm 0.067(\mathrm{syst}))\%. \quad (44)$$

We obtain the final value of $A^b_{\rm sl}(\mathrm{IP}_{>120})$ using the linear combination of Eq. (13), and select the value of α to minimize the total uncertainty on $A^b_{\rm sl}$, which corresponds to $\alpha = -9.29$. The combination for a negative value of α is equivalent to the weighted average of Eqs. (43) and (44) taking into account the correlation of uncertainties (see the Appendix for more details). The corresponding asymmetry $A^b_{\rm sl}$ is found to be

$$A^b_{\rm sl}(\mathrm{IP}_{>120}) = (-0.579 \pm 0.210(\mathrm{stat}) \pm 0.094(\mathrm{syst}))\%. \quad (45)$$

The contributions to the uncertainties in Eqs. (43)–(45) are given in Table XIX.

TABLE XVIII. Input quantities for the measurement of $A^b_{\rm sl}$ using muons with IP above and below 120 μm. Only statistical uncertainties are given.

Quantity	IP $>$ 120 μm	IP $<$ 120 μm
$f_K \times 10^2$	5.19 ± 0.37	17.64 ± 0.27
$f_\pi \times 10^2$	5.65 ± 0.40	34.72 ± 1.86
$f_p \times 10^2$	0.05 ± 0.03	0.45 ± 0.20
$F_K \times 10^2$	4.48 ± 4.05	21.49 ± 0.62
$F_\pi \times 10^2$	4.43 ± 3.95	40.47 ± 2.26
$F_p \times 10^2$	0.03 ± 0.05	0.59 ± 0.23
$f_S \times 10^2$	89.11 ± 0.88	47.18 ± 2.03
$F_{\rm bkg} \times 10^2$	8.94 ± 8.26	62.56 ± 3.07
$F_{SS} \times 10^2$	91.79 ± 7.65	53.66 ± 2.68
$a \times 10^2$	−0.014 ± 0.005	+0.835 ± 0.002
$a_{\rm bkg} \times 10^2$	+0.027 ± 0.023	+0.864 ± 0.049
$A \times 10^2$	−0.529 ± 0.120	+0.555 ± 0.060
$A_{\rm bkg} \times 10^2$	−0.127 ± 0.093	+0.829 ± 0.077
C_π	0.70 ± 0.05	0.95 ± 0.02
C_K	0.39 ± 0.06	0.98 ± 0.01
$F_{LL}/(F_{LL} + F_{SL})$	0.089 ± 0.062	0.350 ± 0.029
c_b	0.109 ± 0.011	0.038 ± 0.007
C_b	0.526 ± 0.037	0.413 ± 0.032

TABLE XIX. Sources of uncertainty on $A^b_{\rm sl}(\mathrm{IP}_{>120})$ in Eqs. (43)–(45). The first nine rows contain statistical uncertainties, and the next four rows contain systematic uncertainties.

Source	$\delta(A^b_{\rm sl}) \times 10^2$ Eq. (43)	$\delta(A^b_{\rm sl}) \times 10^2$ Eq. (44)	$\delta(A^b_{\rm sl}) \times 10^2$ Eq. (45)
A or a (stat)	0.055	0.244	0.093
f_K (stat)	0.048	0.031	0.058
R_K (stat)	N/A	0.244	0.074
$P(\pi \to \mu)/P(K \to \mu)$	0.007	0.004	0.006
$P(p \to \mu)/P(K \to \mu)$	0.012	0.004	0.010
A_K	0.023	0.012	0.017
A_π	0.037	0.009	0.026
A_p	0.025	0.007	0.019
δ or Δ	0.210	0.075	0.157
f_K (syst)	0.112	0.027	0.083
R_K (syst)	N/A	0.014	0.007
π, K, p multiplicity	0.016	0.016	0.016
c_b or C_b	0.043	0.057	0.041
Total statistical	0.240	0.342	0.210
Total systematic	0.121	0.067	0.094
Total	0.269	0.348	0.230

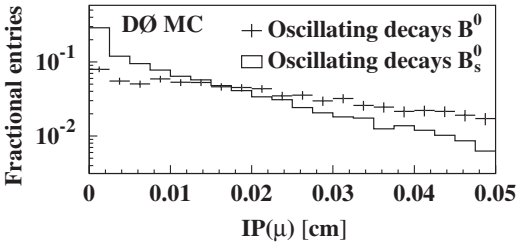

FIG. 20. The normalized IP distribution for muons produced in oscillating decays of B^0 mesons (points with error bars) and B_s^0 mesons (solid histogram) in simulation.

From the known frequencies of oscillations, $\Delta M_q/2\pi$ ($q = d$, s), the period of oscillation for the B^0 meson is many times longer than its lifetime so that the mixing probability of B^0 mesons effectively increases with long decay lengths and large impact parameters. The B_s^0 meson oscillates a number of times within its lifetime so that it is ''fully mixed'' for any appreciable impact parameter requirement. As a result, the fraction of B^0 mesons that have oscillated into the other flavor is increased in the sample with large muon impact parameter. This behavior is demonstrated in Fig. 20, which shows the normalized IP distributions for muons produced in oscillating decays of B^0 and B_s^0 mesons in simulation. The contribution of the $a_{\rm sl}^d$ asymmetry in $A_{\rm sl}^b$ is therefore enhanced in the sample with a large muon IP. From simulation, the mixing probability of B^0 meson in the $\mathrm{IP}_{>120}$ sample is determined to be

$$\chi_d(\mathrm{IP}_{>120}, \mathrm{MC}) = 0.342 \pm 0.004, \quad (46)$$

with the uncertainty limited by the number of simulated events. This value can be compared to the input to the simulation for the B^0 mixing probability integrated over time, $\chi_d = 0.1864 \pm 0.0022$ [3]. The coefficients C_d and C_s in Eq. (2) for the $\mathrm{IP}_{>120}$ selection become

$$\begin{aligned} C_d(\mathrm{IP}_{>120}) &= 0.728 \pm 0.018, \\ C_s(\mathrm{IP}_{>120}) &= 0.272 \pm 0.018. \end{aligned} \quad (47)$$

The value of $A_{\rm sl}^b(\mathrm{IP}_{>120})$ should therefore be reduced relative to the value for the full dimuon sample, if the contribution of $a_{\rm sl}^s$ dominates the asymmetry $A_{\rm sl}^b$.

The measurement of $\mathrm{IP}_{<120}$ is performed using 1.687×10^9 muons in the inclusive-muon sample and 2.857×10^6 events in the like-sign dimuon sample. Exactly the same procedure is applied as for the main measurement, using the background and muon reconstruction asymmetries given in Tables VII and VIII. All other quantities are given in Table XVIII. The background fractions are significantly increased in the samples with small muon IP, thereby increasing the uncertainties related to the background description (Table XX).

Using these values we obtain from the inclusive-muon sample

$$A_{\rm sl}^b(\mathrm{IP}_{<120}) = (-1.65 \pm 2.77(\mathrm{stat}) \pm 4.96(\mathrm{syst}))\%, \quad (48)$$

and from the like-sign dimuon sample

$$A_{\rm sl}^b(\mathrm{IP}_{<120}) = (-1.17 \pm 0.44(\mathrm{stat}) \pm 0.59(\mathrm{syst}))\%. \quad (49)$$

The measurement using the linear combination given in Eq. (13) is performed with $\alpha = +1.27$, which minimizes the total uncertainty on $A_{\rm sl}^b$. The value of $A_{\rm sl}^b$ is found to be

$$A_{\rm sl}^b(\mathrm{IP}_{<120}) = (-1.14 \pm 0.37(\mathrm{stat}) \pm 0.32(\mathrm{syst}))\%. \quad (50)$$

The mean mixing probability χ_d in the $\mathrm{IP}_{<120}$ sample obtained in simulation is found to be

$$\chi_d(\mathrm{IP}_{<120}, \mathrm{MC}) = 0.084 \pm 0.002, \quad (51)$$

and the coefficients C_d and C_s in Eq. (2) for the $\mathrm{IP}_{<120}$ selection are

$$\begin{aligned} C_d(\mathrm{IP}_{<120}) &= 0.397 \pm 0.022, \\ C_s(\mathrm{IP}_{<120}) &= 0.603 \pm 0.022. \end{aligned} \quad (52)$$

The measurements with $\mathrm{IP}_{<120}$ and $\mathrm{IP}_{>120}$ use independent data samples, and the dependence of $A_{\rm sl}^b$ on $a_{\rm sl}^d$ and $a_{\rm sl}^s$ is different for the $\mathrm{IP}_{<120}$ and $\mathrm{IP}_{>120}$ samples. The measurements given in Eqs. (45) and (50) can therefore be

TABLE XX. Sources of uncertainty on $A_{\rm sl}^b(\mathrm{IP}_{<120})$ in Eqs. (48)–(50). The first nine rows contain statistical uncertainties, the next four rows contain systematic uncertainties.

Source	$\delta(A_{\rm sl}^b) \times 10^2$ Eq. (48)	$\delta(A_{\rm sl}^b) \times 10^2$ Eq. (49)	$\delta(A_{\rm sl}^b) \times 10^2$ Eq. (50)
A or a (stat)	0.136	0.233	0.285
f_K (stat)	1.059	0.173	0.082
R_K (stat)	N/A	0.141	0.155
$P(\pi \to \mu)/P(K \to \mu)$	0.388	0.060	0.026
$P(p \to \mu)/P(K \to \mu)$	0.699	0.064	0.004
A_K	0.986	0.123	0.089
A_π	1.727	0.165	0.075
A_p	1.261	0.123	0.050
δ or Δ	0.606	0.107	0.071
f_K (syst)	4.951	0.508	0.034
R_K (syst)	N/A	0.286	0.307
π, K, p multiplicity	0.137	0.034	0.025
c_b or C_b	0.305	0.087	0.093
Total statistical	2.774	0.439	0.366
Total systematic	4.962	0.590	0.323
Total	5.685	0.735	0.488

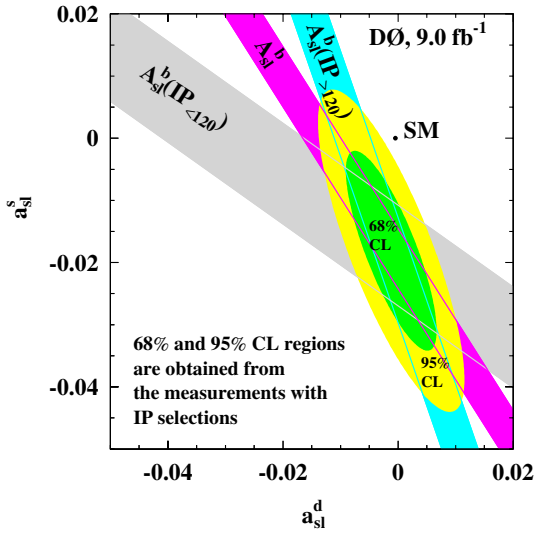

FIG. 21 (color online). Measurements of $A_{\rm sl}^b$ with different muon IP selections in the $(a_{\rm sl}^d, a_{\rm sl}^s)$ plane. The bands represent the ± 1 standard deviation uncertainties on each individual measurement. The ellipses represent the 68% and 95% two-dimensional CL regions, respectively, of $a_{\rm sl}^s$ and $a_{\rm sl}^s$ values obtained from the measurements with IP selections.

combined to obtain the values of $a_{\rm sl}^d$ and $a_{\rm sl}^s$, taking into account the correlation among different sources of uncertainty. All uncertainties in Tables XIX and XX, except the statistical uncertainties on a, A, f_K, R_K, $P(\pi \to \mu)/P(K \to \mu)$, and $P(p \to \mu)/P(K \to \mu)$ are treated as fully correlated. The values of $a_{\rm sl}^d$ and $a_{\rm sl}^s$ extracted are

$$a_{\rm sl}^d = (-0.12 \pm 0.52)\%, \quad a_{\rm sl}^s = (-1.81 \pm 1.06)\%. \quad (53)$$

The correlation ρ_{ds} between these two quantities is

$$\rho_{ds} = -0.799. \quad (54)$$

The uncertainty on $a_{\rm sl}^d$ and $a_{\rm sl}^s$ obtained in this study is comparable with that obtained from the direct measurements. Figure 21 presents the results of the IP study in the $(a_{\rm sl}^d, a_{\rm sl}^s)$ plane together with the result (36) of the $A_{\rm sl}^b$ measurement using all like-sign dimuon events. The ellipses represent the 68% and 95% two-dimensional confidence level (CL) regions, respectively, of $a_{\rm sl}^s$ and $a_{\rm sl}^s$ values obtained from the measurements with IP selections.

We also performed four additional measurements with IP thresholds of 50 μm and 80 μm. They are denoted as $\rm IP_{<50}$, $\rm IP_{>50}$, $\rm IP_{<80}$, and $\rm IP_{>80}$, respectively. The input quantities for these measurements are presented in Tables XXI and XXII. The $A_{\rm sl}^b$ values in the inclusive and like-sign dimuon samples and their combinations are given in Table XXIII. The mean mixing probability χ_d for all these measurement is obtained through simulation. The results are presented in Table XXIV, together with the corresponding coefficients C_d and C_s.

TABLE XXI. Input quantities for the measurement of $A_{\rm sl}^b$ using muons with IP above 50 μm, 80 μm and 120 μm, respectively. Only statistical uncertainties are given.

Quantity	IP $>$ 50 μm	IP $>$ 80 μm	IP $>$ 120 μm
$f_K \times 10^2$	6.47 ± 0.18	5.38 ± 0.24	5.19 ± 0.37
$f_\pi \times 10^2$	10.42 ± 0.47	7.24 ± 0.38	5.65 ± 0.40
$f_p \times 10^2$	0.11 ± 0.05	0.07 ± 0.03	0.05 ± 0.03
$F_K \times 10^2$	6.31 ± 1.73	4.79 ± 2.59	4.48 ± 4.05
$F_\pi \times 10^2$	9.51 ± 2.36	6.39 ± 2.95	4.43 ± 3.95
$F_p \times 10^2$	0.11 ± 0.06	0.03 ± 0.04	0.03 ± 0.05
$f_S \times 10^2$	82.99 ± 0.81	87.32 ± 0.74	89.11 ± 0.88
$F_{\rm bkg} \times 10^2$	15.91 ± 4.38	11.39 ± 6.10	8.94 ± 8.26
$F_{SS} \times 10^2$	85.63 ± 3.74	89.88 ± 5.10	91.79 ± 7.65
$a \times 10^2$	+0.134 ± 0.004	+0.035 ± 0.005	−0.014 ± 0.005
$a_{\rm bkg} \times 10^2$	+0.146 ± 0.024	+0.068 ± 0.023	+0.027 ± 0.023
$A \times 10^2$	−0.302 ± 0.079	−0.386 ± 0.094	−0.529 ± 0.120
$A_{\rm bkg} \times 10^2$	−0.043 ± 0.071	−0.139 ± 0.083	−0.127 ± 0.093
C_π	0.81 ± 0.03	0.75 ± 0.05	0.70 ± 0.05
C_K	0.66 ± 0.03	0.52 ± 0.05	0.39 ± 0.06
$\frac{F_{LL}}{(F_{LL}+F_{SL})}$	0.108 ± 0.038	0.125 ± 0.060	0.089 ± 0.062
c_b	0.084 ± 0.008	0.095 ± 0.009	0.109 ± 0.011
C_b	0.496 ± 0.034	0.510 ± 0.034	0.526 ± 0.037

As for the combinations of the $\rm IP_{<120}$ and $\rm IP_{>120}$ samples, the measurements with $\rm IP_{<50}$ and $\rm IP_{>50}$ samples, as well as with $IP_{<80}$ and $IP_{>80}$ samples, can be combined to determine the values of $a_{\rm sl}^d$ and $a_{\rm sl}^s$ (Table XXV). The measurements with different IP thresholds are consistent with each other within 2 standard deviations taking into account the correlation between the uncertainties.

TABLE XXII. Input quantities for the measurement of $A_{\rm sl}^b$ using muons with IP below 50 μm, 80 μm and 120 μm, respectively. Only statistical uncertainties are given.

Quantity	IP $<$ 50 μm	IP $<$ 80 μm	IP $<$ 120 μm
$f_K \times 10^2$	19.35 ± 0.33	18.32 ± 0.30	17.64 ± 0.27
$f_\pi \times 10^2$	37.58 ± 2.08	34.34 ± 1.95	34.72 ± 1.86
$f_p \times 10^2$	0.51 ± 0.22	0.48 ± 0.21	0.45 ± 0.20
$F_K \times 10^2$	28.03 ± 0.95	23.79 ± 0.74	21.49 ± 0.62
$F_\pi \times 10^2$	51.72 ± 3.18	44.26 ± 2.63	40.47 ± 2.26
$F_p \times 10^2$	0.77 ± 0.29	0.66 ± 0.25	0.59 ± 0.23
$f_S \times 10^2$	42.56 ± 2.73	45.40 ± 2.13	47.18 ± 2.03
$F_{\rm bkg} \times 10^2$	81.53 ± 4.30	70.13 ± 3.52	62.56 ± 3.07
$F_{SS} \times 10^2$	43.42 ± 3.75	48.76 ± 2.84	53.66 ± 2.68
$a \times 10^2$	+0.953 ± 0.003	+0.896 ± 0.003	+0.835 ± 0.002
$a_{\rm bkg} \times 10^2$	+0.997 ± 0.056	+0.916 ± 0.052	+0.864 ± 0.049
$A \times 10^2$	+0.715 ± 0.083	+0.683 ± 0.069	+0.555 ± 0.060
$A_{\rm bkg} \times 10^2$	+1.243 ± 0.096	+0.994 ± 0.082	+0.829 ± 0.077
C_π	0.97 ± 0.01	0.95 ± 0.02	0.95 ± 0.02
C_K	0.99 ± 0.01	0.98 ± 0.01	0.98 ± 0.01
$\frac{F_{LL}}{(F_{LL}+F_{SL})}$	0.441 ± 0.050	0.369 ± 0.032	0.350 ± 0.029
c_b	0.033 ± 0.007	0.035 ± 0.007	0.038 ± 0.007
C_b	0.406 ± 0.032	0.406 ± 0.032	0.413 ± 0.032

TABLE XXIII. Values of $A^b_{\rm sl}$ with their statistical and systematic uncertainties obtained for different IP selections.

Selection	Sample	Central value $\times 10^2$	Uncertainty $\times 10^2$ statistical	systematic
All events	1μ	-1.042	1.304	2.313
	2μ	-0.808	0.202	0.222
	comb.	-0.787	0.172	0.093
IP <50 μm	1μ	-3.244	4.101	7.466
	2μ	-2.837	0.776	1.221
	comb.	-2.779	0.674	0.694
IP >50 μm	1μ	-0.171	0.343	0.311
	2μ	-0.593	0.257	0.074
	comb.	-0.533	0.239	0.100
IP <80 μm	1μ	-1.293	3.282	5.841
	2μ	-1.481	0.541	0.810
	comb.	-1.521	0.458	0.501
IP >80 μm	1μ	-0.388	0.280	0.179
	2μ	-0.529	0.285	0.048
	comb.	-0.472	0.226	0.091
IP <120 μm	1μ	-1.654	2.774	4.962
	2μ	-1.175	0.439	0.590
	comb.	-1.138	0.366	0.323
IP >120 μm	1μ	-0.422	0.240	0.121
	2μ	-0.818	0.342	0.067
	comb.	-0.579	0.210	0.094

TABLE XXIV. Mean mixing probability (χ_d) obtained in simulation, and the coefficients C_d and C_s in Eq. (2), used for different selections.

Sample	χ_d(MC)	C_d	C_s
$\rm IP_{<50}$	0.059 ± 0.002	0.316 ± 0.021	0.684 ± 0.021
$\rm IP_{<80}$	0.069 ± 0.002	0.351 ± 0.022	0.649 ± 0.022
$\rm IP_{<120}$	0.084 ± 0.002	0.397 ± 0.022	0.603 ± 0.022
$\rm IP_{>50}$	0.264 ± 0.004	0.674 ± 0.020	0.326 ± 0.020
$\rm IP_{>80}$	0.299 ± 0.004	0.701 ± 0.019	0.299 ± 0.019
$\rm IP_{>120}$	0.342 ± 0.004	0.728 ± 0.018	0.272 ± 0.018

TABLE XXV. Measured values of $a^d_{\rm sl}$ nd $a^s_{\rm sl}$ for different muon IP thresholds. In each column, the measurements using the samples with muon IP larger and smaller than the given threshold are combined. We also give the correlation ρ_{ds} between $a^d_{\rm sl}$ and $a^s_{\rm sl}$.

Quantity	muon IP threshold 50 μm	80 μm	120 μm
$a^d_{\rm sl} \times 10^2$	$+1.51 \pm 0.93$	$+0.42 \pm 0.68$	-0.12 ± 0.52
$a^s_{\rm sl} \times 10^2$	-4.76 ± 1.79	-2.57 ± 1.34	-1.81 ± 1.06
ρ_{ds}	-0.912	-0.857	-0.799

We conclude that the observed dependence of the like-sign dimuon charge asymmetry on muon IP is consistent with the hypothesis that it has its origin from semileptonic b-hadron decays. The contributions of $a^d_{\rm sl}$ and $a^s_{\rm sl}$ to $A^b_{\rm sl}$ can be determined separately by dividing the sample according to the muon IP, although the uncertainties on the values of $a^d_{\rm sl}$ and $a^s_{\rm sl}$ do not allow for the definitive conclusion that the deviation of $A^b_{\rm sl}$ from its SM prediction is dominated from the $a^s_{\rm sl}$ asymmetry.

XV: CONCLUSIONS

We have presented an update to the previous measurement [11] of the anomalous like-sign dimuon charge asymmetry $A^b_{\rm sl}$ with 9.0 fb^{-1} of integrated luminosity. The analysis has improved criteria for muon selection, which provide a stronger background suppression and increase the size of the like-sign dimuon sample. A more accurate measurement of the fraction of kaons that produce muons in the inclusive-muon sample (f_K), and an additional measurement of the ratio of such yields in like-sign dimuon to inclusive-muon data ($R_K = F_K/f_K$) using $K^0_S \to \pi^+\pi^-$ decay have been performed. This provides better precision of R_K, and an independent estimate of the systematic uncertainty on this quantity. The value of the like-sign dimuon charge asymmetry $A^b_{\rm sl}$ in semileptonic b-hadron decays is found to be

$$A^b_{\rm sl} = (-0.787 \pm 0.172(\text{stat}) \pm 0.093(\text{syst}))\%. \quad (55)$$

This measurement disagrees with the prediction of the standard model by 3.9 standard deviations and provides evidence for anomalously large CP violation in semileptonic neutral B decay. The residual charge asymmetry of like-sign dimuon events after taking into account all background sources is found to be

$$A_{\rm res} = (-0.246 \pm 0.052(\text{stat}) \pm 0.021(\text{syst}))\%. \quad (56)$$

It differs by 4.2 standard deviations from the standard model prediction.

Separation of the sample by muon impact parameter allows for separate extraction of $a^d_{\rm sl}$ and $a^s_{\rm sl}$. We obtain

$$a^d_{\rm sl} = (-0.12 \pm 0.52)\%, \qquad a^s_{\rm sl} = (-1.81 \pm 1.06)\%. \quad (57)$$

The correlation ρ_{ds} between these two quantities is

$$\rho_{ds} = -0.799. \quad (58)$$

The uncertainties on $a^d_{\rm sl}$ and $a^s_{\rm sl}$ do not allow for the definitive conclusion that $a^s_{\rm sl}$ dominates the value of $A^b_{\rm sl}$.

Our results are consistent with the hypothesis that the anomalous like-sign dimuon charge asymmetry arises from semileptonic b-hadron decays. The significance of the difference of this measurement with the SM prediction is not sufficient to claim observation of physics beyond the

standard model, but it has grown compared to our previous measurement with a smaller data sample.

ACKNOWLEDGMENTS

We thank the staffs at Fermilab and collaborating institutions, and acknowledge support from the DOE and NSF (USA); CEA and CNRS/IN2P3 (France); FASI, Rosatom and RFBR (Russia); CNPq, FAPERJ, FAPESP and FUNDUNESP (Brazil); DAE and DST (India); Colciencias (Colombia); CONACyT (Mexico); KRF and KOSEF (Korea); CONICET and UBACyT (Argentina); FOM (The Netherlands); STFC and the Royal Society (United Kingdom); MSMT and GACR (Czech Republic); CRC Program and NSERC (Canada); BMBF and DFG (Germany); SFI (Ireland); The Swedish Research Council (Sweden); and CAS and CNSF (China).

APPENDIX A: COMBINATION OF TWO MEASUREMENTS USING α SCAN

In this analysis, the value of $A_{\rm sl}^b$ is obtained from the linear combination in Eq. (13). The parameter α is selected to minimize the total uncertainty on $A_{\rm sl}^b$, taking into account the correlation among different contributions to the uncertainty on $A_{\rm sl}^b$. This procedure is equivalent to the standard procedure of taking a weighted average.

To demonstrate this, we consider a model in which we obtain the quantity x using two measurements a and A. Suppose that a and A depend linearly on x

$$a = kx + b, \qquad A = Kx + B, \tag{A1}$$

where k, K, b, and B are parameters determined in the analysis, and correspond to the measurement of $A_{\rm sl}^b$. Using the measurements of a and A, we obtain two estimates of x

$$x_1 = (a - b)/k, \qquad x_2 = (A - B)/K. \tag{A2}$$

We denote the uncertainties on x_1 and x_2 as σ_1 and σ_2, respectively.

Consider the case where the measurements of a and A, as well as the uncertainties σ_1 and σ_2, are statistically independent. In this case, the value of x can be obtained as a weighted average

$$x = (w_1 x_1 + w_2 x_2)/w, \qquad w_i = 1/\sigma_i^2, \quad i = 1, 2, \qquad w = 1/\sigma_1^2 + 1/\sigma_2^2. \tag{A3}$$

Consider another estimate of x using the difference

$$A' = A - \alpha a, \tag{A4}$$

where α is a free parameter. The value of x obtained from Eq. (A4) is

$$x = \frac{(A - B) - \alpha(a - b)}{K - \alpha k}. \tag{A5}$$

Provided that the two measurements a and A, as well as the uncertainties σ_1 and σ_2 are statistically independent, the minimal uncertainty on x is obtained for

$$\alpha_{\rm min} = -(K\sigma_2^2)/(k\sigma_1^2). \tag{A6}$$

The central value and uncertainty on x obtained from Eq. (A5), with $\alpha = \alpha_{\rm min}$, are exactly the same as the central value and uncertainty obtained from the weighted average (A3). This case is similar to the combination (45) of the two measurements with IP > 120 μm that have reduced correlations. The coefficient α in this case is negative, and its value depends on the uncertainties σ_1 and σ_2.

Consider another extreme case, where $k = 0$ and B is fully correlated with b, e.g., $B = Cb$, where C is a coefficient. In this case, the value of x obtained from Eq. (A5) is equal to

$$x = \frac{A - \alpha a - (C - \alpha)b}{K}. \tag{A7}$$

Provided that $\sigma(a) \ll \sigma(A)$, the minimal uncertainty of x is obtained for $\alpha_{\rm min} = C$. This case corresponds to the measurement of Eq. (36) with the full data sample. The value of $\alpha_{\rm min}$ is positive for $C > 0$.

These two examples demonstrate that the method of the α scan used in this analysis is equivalent to the weighted average of two measurements, taking into account the correlation among different uncertainties.

[1] Charge conjugate states are implied throughout this article.
[2] Y. Grossman *et al.*, Phys. Rev. Lett. **97**, 151801 (2006).
[3] D. Asner *et al.*, Heavy Flavor Averaging Group (HFAG), arXiv:1010.1589.
[4] CDF Collaboration, Public Note 10335, 2011; http://www-cdf.fnal.gov/physics/new/bottom/110127.blessed-chibar/
[5] A. Lenz and U. Nierste, J. High Energy Phys. 06 (2007) 072.
[6] L. Randall and S. Su, Nucl. Phys. **B540**, 37 (1999).
[7] J. L. Hewett, arXiv:hep-ph/9803370.
[8] G. W. S. Hou, arXiv:0810.3396.
[9] A. Soni *et al.*, Phys. Lett. B **683**, 302 (2010); Phys. Rev. D **82**, 033009 (2010), and references therein.
[10] M. Blanke *et al.*, J. High Energy Phys. 12 (2006) 003; W. Altmannshofer *et al.*, Nucl. Phys. **B830**, 17 (2010).

[11] V. M. Abazov *et al.* (D0 Collaboration), Phys. Rev. D **82**, 032001 (2010); Phys. Rev. Lett. **105**, 081801 (2010).
[12] The impact parameter is defined here as the distance of closest approach to a given vertex of the projection of a particle's trajectory on the plane perpendicular to the direction of the beam.
[13] V. M. Abazov *et al.* (D0 Collaboration), Nucl. Instrum. Methods Phys. Res., Sect. A **565**, 463 (2006); **552**, 372 (2005); S. N. Ahmed *et al.*, Nucl. Instrum. Methods Phys. Res., Sect. A **634**, 8 (2011); R. Angstadt *et al.*, Nucl. Instrum. Methods Phys. Res., Sect. A **622**, 298 (2010).
[14] K. Nakamura *et al.*, J. Phys. G **37**, 075021 (2010).
[15] The D0 detector utilizes a right-handed coordinate system with the z axis pointing in the direction of the proton beam and the y axis pointing upwards. The azimuthal angle is defined in the xy plane measured from the x axis. The pseudorapidity is defined as $\eta \equiv -\ln[\tan(\theta/2)]$, where θ is the polar angle with respect to the proton beam direction.
[16] V. M. Abazov *et al.* (D0 Collaboration), Phys. Rev. D **74**, 092001 (2006).
[17] The notation and definition of all quantities are given in Ref. [11].
[18] A. Mitov, Phys. Rev. D **84**, 014035 (2011).
[19] V. M. Abazov *et al.* (D0 Collaboration), Phys. Rev. D **82**, 012003 (2010).
[20] M. Gronau and J. L. Rosner, Phys. Rev. D **82**, 077301 (2010).